Geochemistry, Geophysics, Geosystems

RESEARCH ARTICLE
10.1029/2019GC008876

Key Points:
- The formation of Paleogene and Miocene broken foreland basins segmented the Andean retroarc
- Inherited structures controlled the formation and the evolution of broken foreland basins
- Slab anchoring may have promoted retroarc deformation

Supporting Information:
- Supporting Information S1
- Table S4

Correspondence to:
S. Zapata,
szapatah@gmail.com

Citation:
Zapata, S., Sobel, E. R., Del Papa, C., & Glodny, J. (2020). Upper plate controls on the formation of broken foreland basins in the Andean retroarc between 26°S and 28°S: From Cretaceous rifting to Paleogene and Miocene broken foreland basins. *Geochemistry, Geophysics, Geosystems*, *21*, e2019GC008876. https://doi.org/10.1029/2019GC008876

Received 30 DEC 2019
Accepted 29 MAY 2020
Accepted article online 2 JUN 2020

Upper Plate Controls on the Formation of Broken Foreland Basins in the Andean Retroarc Between 26°S and 28°S: From Cretaceous Rifting to Paleogene and Miocene Broken Foreland Basins

S. Zapata[1], E. R. Sobel[1], C. Del Papa[2], and J. Glodny[3]

[1]Institute of Geosciences, University of Potsdam, Potsdam, Germany, [2]Cicterra, CONICET-University of Cordoba, Cordoba, Argentina, [3]GFZ German Research Centre for Geosciences, Potsdam, Germany

Abstract Marked along-strike changes in stratigraphy, mountain belt morphology, basement exhumation, and deformation styles characterize the Andean retroarc; these changes have previously been related to spatiotemporal variations in the subduction angle. We modeled new apatite fission track and apatite (U-Th-Sm)/He data from nine ranges located between 26°S and 28°S. Using new and previously published data, we constructed a Cretaceous to Pliocene paleogeographic model that delineates a four-stage tectonic evolution: extensional tectonics during the Cretaceous (120–75 Ma), the formation of a broken foreland basin between 55 and 30 Ma, reheating due to burial beneath sedimentary rocks (18–13 Ma), and deformation, exhumation, and surface uplift during the Late Miocene and the Pliocene (13–3 Ma). Our model highlights how preexisting upper plate structures control the deformation patterns of broken foreland basins. Because retroarc deformation predates flat-slab subduction, we propose that slab anchoring may have been the precursor of Eocene–Oligocene compression in the Andean retroarc. Our model challenges models which consider broken foreland basins and retroarc deformation in the NW Argentinian Andes to be directly related to Miocene flat subduction.

1. Introduction

Cordilleran orogens, such as the Andes, are characterized by subduction of an oceanic plate beneath continental lithosphere (DeCelles et al., 2009). During subduction, contractional or extensional phases are controlled by the relative convergence rate, angle of subduction, and the contrast between the densities of the subducting slab and the mantle (Chen et al., 2019; Horton, 2018b; Oncken et al., 2006). However, the controls exerted by the subduction system on upper plate deformation and sedimentation patterns remain controversial (Horton, 2018b; Jordan et al., 1983; Kley et al., 1999). The Andes are characterized by spatial (along-strike) and temporal variations in the deformation patterns that are responsible for changes in mountain belt morphology, magnitude of shortening, and foreland basin geometry (Figure 1a) (e.g., Jordan et al., 1983; Pearson et al., 2012). Several authors proposed different conditions such as flat subduction, interactions between the slab and the mantle, and upper plate inherited structures to be the main precursor of these spatiotemporal variations along the Andes (e.g., Chen et al., 2019; Horton, 2018b; Martinod et al., 2020; Pearson et al., 2013).

Flat-slab subduction increases plate coupling, which promotes deformation toward the foreland and upper plate compression (e.g., Horton, 2018b; Martinod et al., 2020). Moreover, the penetration of the subducted slab into the lower mantle also increases plate coupling and promotes upper plate shortening (Chen et al., 2019; Faccenna et al., 2017). Diachronic flat-slab subduction along the Andean continental margin has been suggested to be the main precursor of thick-skin retroarc deformation and therefore may be responsible for variations in foreland basin geometries, deformation patterns, and mountain belt morphology (e.g., Horton, 2018b; Jordan et al., 1983; Martinod et al., 2020; Ramos, 2009). Alternatively, several authors have proposed that inherited structures controlled the geometry of foreland basins and along-strike segmentation of the Andean retroarc (del Papa et al., 2013; Kley & Monaldi, 2002; Pearson et al., 2013). We aim to better understand the evolution of the Andean retroarc by documenting

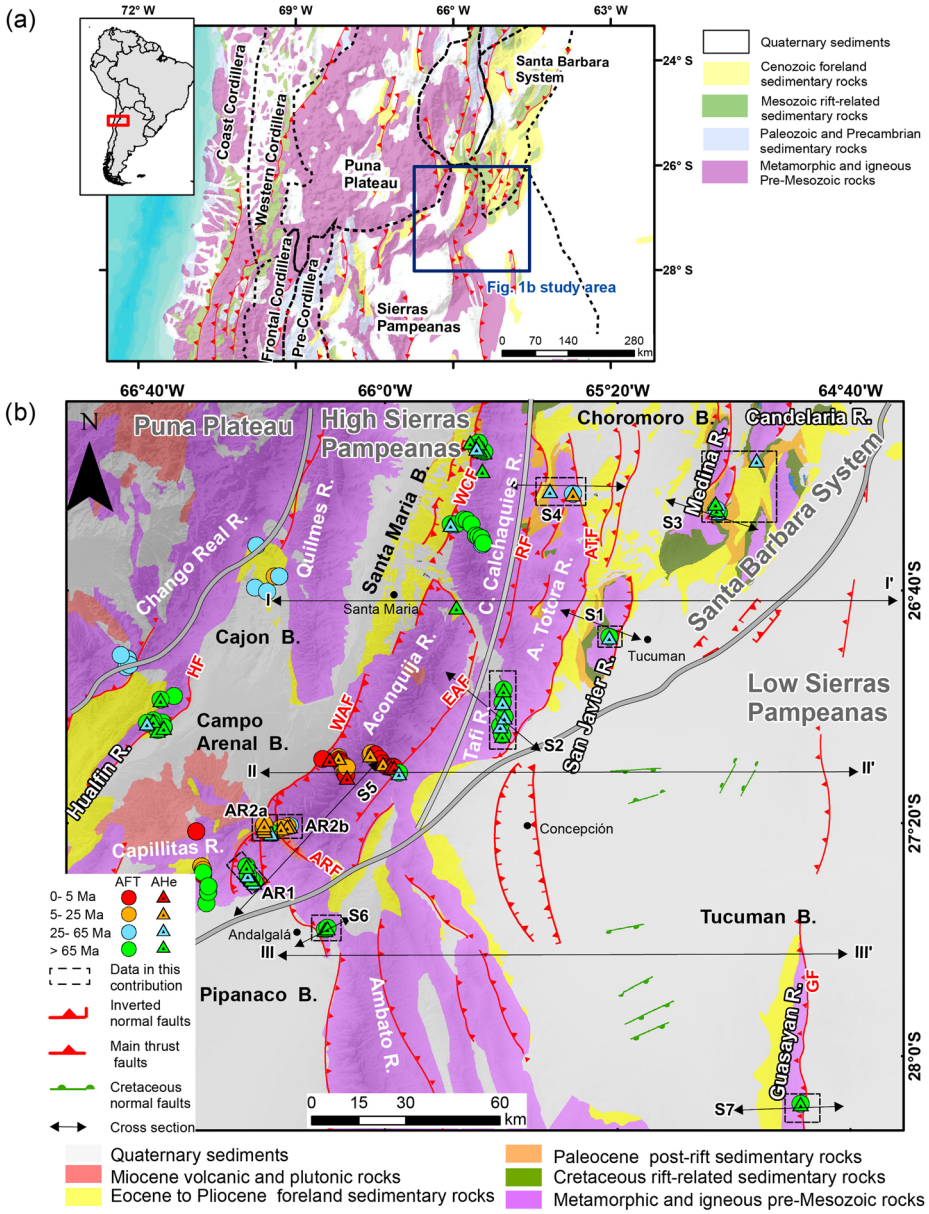

Figure 1. (a) Central Andes sedimentary cover and geological provinces modified from Kley et al. (1999). (b) Geological map of the study area modified from Dal Molin et al. (2003) and González (2000), showing available thermochronology ages (Coughlin et al., 1999; Coutand et al., 2006; Löbens et al., 2013; Mortimer et al., 2007; Sobel & Strecker, 2003; Zapata et al., 2019b). Color code denotes ages; circles represent AFT, triangles are AHe, and dashed black squares contain the new ages presented in this contribution. Gray lines denote the limits of the different tectonomorphic provinces. Faults within the Tucuman Basin were taken from seismic-based reconstructions (Iaffa et al., 2011, 2013). HF: Hualfin fault; WAF: West Aconquija fault; ARF: Agua Rica fault; EAF: East Aconquija fault, ATF: Altos del Tortora fault; RF: Rearte fault; and GF: Guasayan fault. Letter "S" relates to the sections presented in Figure 2.

the spatiotemporal relationships between deformation patterns, inherited structures, and previously documented variations in the subduction angle.

Between 26°S and 28°S, the Puna Plateau and the associated Santa Barbara broken foreland abruptly terminates and transitions southward into the Sierras Pampeanas broken foreland. To constrain the timing of segmentation in this portion of the Andean broken foreland, we reconstruct and compare the thermal histories of nine basement blocks in the Santa Barbara system and Sierras Pampeanas using apatite fission-track (AFT) and apatite (U-Th-Sm)/He (AHe) data. We use new and published thermochronometric data to

develop a Cretaceous to Pliocene paleogeographic model of the Andean retroarc. We document Paleogene and Miocene retroarc deformation that may have been promoted by slab penetration into the lower mantle and flat-slab subduction, respectively. During these contractional phases, inherited structures controlled the deformation patterns and basin geometries.

2. Geological Background

2.1. Tectonic Evolution of the Central Andes

Foreland basin geometries can be divided into two end-member styles (Strecker et al., 2011). Continuous foreland basin systems are associated with thin-skin deformation related to the growth of an orogenic wedge (DeCelles & Giles, 1996; Horton & DeCelles, 1997). Conversely, broken foreland basins are characterized by thick-skin deformation (Jordan & Allmendinger, 1986; Strecker et al., 2011). This study targets samples collected along the transition between the high elevation Puna Plateau, the Santa Barbara system, and the Sierras Pampeanas tectonomorphic provinces. The Santa Barbara system is a broken foreland basin characterized by combined thick-skin and thin-skin deformation that includes inverted normal faults and shallow décollements in the sedimentary fill (Abascal, 2005; Kley & Monaldi, 2002). The Sierras Pampeanas encompasses several discontinuous mountain ranges bounded by high-angle faults (Jordan & Allmendinger, 1986). The Sierras Pampeanas broken foreland is 5 times broader (E-W ~ 500 km) than the Santa Barbara broken foreland (Figure 1a).

During the Early Cretaceous (130–70 Ma), the Central Andes experienced at least two extensional rifting episodes related to the opening of the South Atlantic Ocean (Marquillas et al., 2005; Moulin et al., 2010). During this period, rift basins developed along the Central Andes, including the Salta Basin exposed in the Santa Barbara system, and the Sierras Chicas and San Luis Basins located to the south of the Sierras Pampeanas (Figure 1a) (Marquillas et al., 2005; Salfity & Marquillas, 1994; Schmidt et al., 1995; Viramonte et al., 1999). Between 70 and 55 Ma, the Central Andes experienced regional thermal subsidence that facilitated the deposition of postrift strata within the Early Cretaceous rift basins (Becker et al., 2015; Marquillas et al., 2005).

Contractional tectonics characterized the Late Cretaceous to Cenozoic evolution of the Central Andes; this has been interpreted to have driven several deformational phases and associated mountain-building events (e.g., Arriagada et al., 2006; Chen et al., 2019; Horton, 2018a; Oncken et al., 2006; Sobolev et al., 2005). In the Central Andean retroarc, shortening and crustal thickening initiated between 50 and 30 Ma (Canavan et al., 2014; Zhou et al., 2017). The Eocene to Oligocene tectonic evolution of the Central Andean retroarc between 25°S and 30°S has been extensively discussed. Several authors postulated that the Central Andean retroarc was undeformed and constituted a distal segment of a continuous foreland basin formed during a period of steep subduction (Carrapa et al., 2008; DeCelles et al., 2011; Gianni et al., 2020; Zhou et al., 2017). Alternative models proposed that Paleogene deformation in the Central Andean retroarc formed disconnected basement highs that characterize a broken foreland basin (del Papa et al., 2013; Hongn et al., 2007; Payrola et al., 2009). In the Sierras Pampeanas and the Santa Barbara system, Miocene deformation was characterized by basement-involved faulting and a broken foreland basin (Dávila et al., 2007; Kley & Monaldi, 2002; Löbens et al., 2013; Pearson et al., 2013). Yáñez et al. (2002) suggested that the collision between the South American margin and the Juan Fernandez Ridge caused flat-slab subduction of the Nazca plate beneath the South American plate during the Miocene. This model predicts that flat-slab subduction commenced beneath the study area (26–28°S) around 12 Ma. However, Gianni et al. (2020) suggested that between 25°S and 28°S flat-slab subduction started at ~26 Ma. The formation of the Sierras Pampeanas and the Santa Barbara broken foreland basins has been directly related to Late-Oligocene to Miocene flat-slab subduction (Carrapa et al., 2008; Gianni et al., 2020; Jordan et al., 1983; Ramos & Folguera, 2009).

2.2. Geology of the Study Area (26–28°S)

Between 26°S and 28°S, the transition from the Puna Plateau and the associated Santa Barbara system to the Sierras Pampeanas is marked by the termination of elevated intermountain basins, changes in fault geometries, variations in the thickness of the sedimentary fill, and variations in the morphology of mountain belts (Figure 1) (Gapais et al., 1996; Löbens et al., 2013; Zapata et al., 2019). Herein, we informally subdivide the Sierras Pampeanas province into two regions: the High and Low Sierras Pampeanas (Figure 1b). The High Sierras Pampeanas (HSP) comprises the Campo-Arenal, El Cajon, and the Santa Maria elevated basins

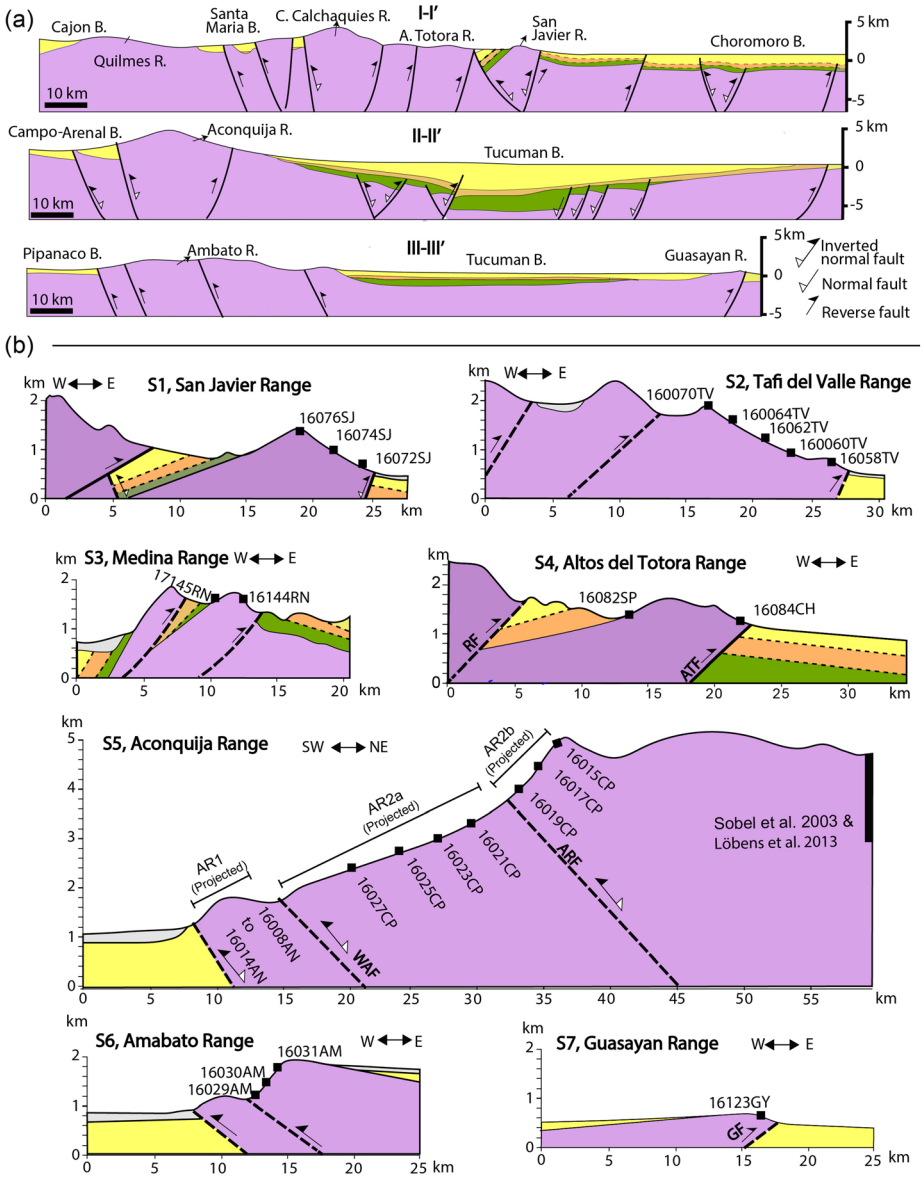

Figure 2. (a) Structural sections modified from Iaffa et al. (2013), vertical exaggeration is 2:1. (b) Schematic cross sections of the studied ranges are based on available geological maps and seismic data presented by Abascal (2005) and Iaffa et al. (2011), vertical exaggeration is 4:1. Dashed black lines denote schematically faults. Locations and color codes are presented in Figure 1b.

(~2,000 masl). The HSP sedimentary fill is characterized by Miocene to Pliocene coarsening-up successions that unconformably overlie either Eocene to Oligocene sedimentary rocks or paleosurfaces (Zapata et al., 2019a, 2019b).

The eastern limit of the HSP is marked by the Aconquija and Cumbres Calchaquies Ranges. The Aconquija Range is a ~5,000-masl basement block bounded by two high-angle NE-striking reverse faults parallel to the trend of the range (Figure 1b) (Cristallini et al., 1997; Löbens et al., 2013); the southern end of this range is characterized by several ~NW-striking faults oriented perpendicular to the trend of the range (Figure 1b) (Seggiaro et al., 2014). The Choromoro Basin marks the southern limit of the Santa Barbara system; this basin hosts syn-rift strata of the Pirgua group deposited between 130 and 70 Ma. Between 70 and 55 Ma, the Balbuena and Santa Barbara groups were deposited during a period of postrift thermal subsidence. These rift-related units are overlain by clastic sedimentary rocks deposited in fluvial and lacustrine settings during the Paleogene (Figure 2a); in the study area, the relation of these units with the post-rift depositional

system or with the early phases of the Andean orogeny is unknown due to the lack of chronostratigraphic constraints (DeCelles et al., 2011; Georgieff et al., 2014; Zapata, et al., 2019a). Finally, Miocene to Pliocene coarsening-up sedimentary successions were unconformably deposited on top of the Paleogene units (Figure 2a) (Zapata et al., 2019a).

West of the Choromoro Basin is the Altos del Totora Range (Figure 1b). This range is bounded to the east by a reverse fault; to the west, the basement of the range is overlain by Paleogene to Cenozoic sedimentary rocks (Abascal, 2005). The Tafi del Valle Range is the southward continuation of the Altos del Totora Range. South of the Choromoro Basin is the San Javier Range, which is bounded by a reverse fault to the east; to the west, the basement of the range is overlain by Cretaceous to Miocene strata. The Medina and Candelaria Ranges are part of the basement-cored eastern ranges; the basement of these ranges is unconformably overlain by Cretaceous to Miocene sedimentary rocks (Figures 1b and 2b).

The Low Sierras Pampeanas (LSP) is formed by the Tucuman and Pipanaco Basins. This subprovince is characterized by low-elevation depocenters (~800 masl); the sedimentary strata in these basins are usually less deformed than the sediments in the HSP (Figure 2a). In the Tucuman Basin, outcrops are restricted to coarsening-up Miocene clastic strata that accumulated in lacustrine and fluvial systems (Zapata et al., 2019a). However, seismic data suggest the presence of undeformed Cretaceous and Paleogene strata (Figure 2a) (Iaffa et al., 2011). Between the Pipanaco and the Tucuman Basins is the ~2,700-masl Ambato Range, which is bounded by a reverse fault to the west. Miocene sedimentary rocks overlie basement rocks of this range (Figure 2b) (Zapata et al., 2019a). In the SE part of the Tucuman Basin is the ~600-masl Guasayan Range, which is delineated by a reverse fault to the east; to the west, the basement of the range is overlain by Miocene sedimentary rocks (Figure 2b) (Dal Molin et al., 2003).

The basement in the study area includes Cambrian to Ordovician schists, gneisses, and migmatites grouped into the Puncoviscana Fm.; all were intruded by Ordovician granites (Adams et al., 2007, 2008; Ramos, 2008 and references therein). Available basement thermochronological data shows contrasting exhumation and tectonic histories in the study area (Figure 1b). The Cumbres Calchaquies, Quilmes, and Capillitas Ranges exhibit Cretaceous AFT and AHe ages interpreted to reflect Cretaceous horst exhumation followed by Miocene reheating and Miocene-Pliocene exhumation (Carrapa et al., 2014; Coughlin et al., 1999; Löbens et al., 2013; Mortimer et al., 2007; Sobel & Strecker, 2003). The Aconquija Range yields Paleogene zircon (U-Th)/He (ZHe) ages and Miocene to Pliocene AFT and AHe ages, indicating an along-strike increase in Miocene exhumation with respect to the Cumbres Calchaquies Range (Figure 1b) (Löbens et al., 2013; Sobel & Strecker, 2003). Finally, the Chango Real Range yields Paleogene AFT ages interpreted to record exhumation during the early phases of the Andean orogeny (Coutand et al., 2001).

3. Methods

3.1. Sampling

We collected 31 samples from nine basement blocks in the study area. Low-grade metamorphic rocks of the Puncoviscana Fm. and Ordovician granitic rocks were collected in vertical transects or from different structural positions within the basement blocks (Figure 3). The relative position of the samples within the rock body allows for the reconstruction of thermal histories (e.g., Reiners & Brandon, 2006).

3.2. AFT Method

The AFT method is based on the quantification of damage to the crystal lattice (tracks) that results from the spontaneous fission of ^{238}U. These tracks are partially annealed at temperatures between ~60°C and 120°C; this interval is known as the apatite partial annealing zone (APAZ) (Wagner et al., 1989). Fission tracks shorten within the APAZ; therefore, the track length distribution (TLD) and the mean track length (MTL) values can be used as proxies to reconstruct the thermal history within the APAZ (Green et al., 1985). The fission-track annealing resistance depends strongly on the kinetics of the apatite crystal. A useful kinetic indicator is the resistance of the crystal to the acid used to reveal the tracks (etching). Therefore, the diameter of the fission-track etch pit (Dpar) can be used as a proxy to quantify resistance to annealing (Carlson et al., 1999; Donelick et al., 1999; Ketcham et al., 1999). The detailed procedures for etching, Dpar measurements, and sample preparation are presented in Text S1 in the supporting information (Dunkl, 2002;

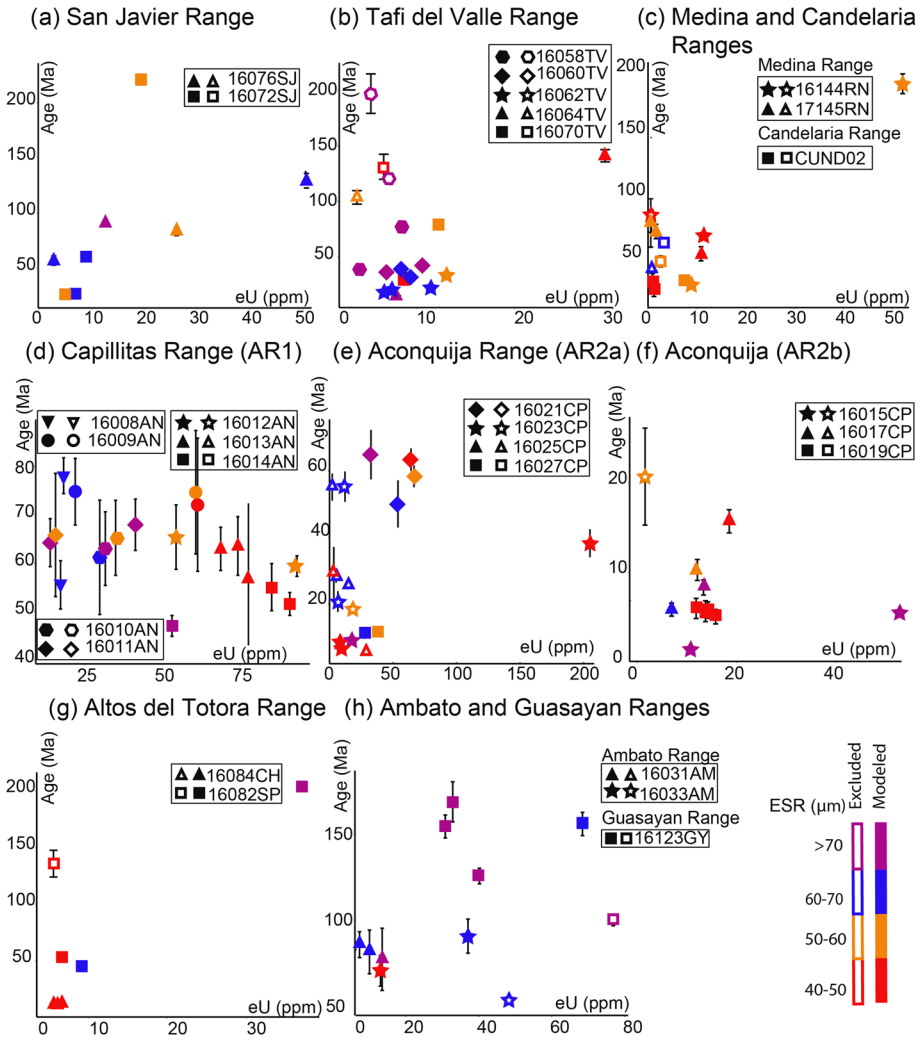

Figure 3. (a–h) eU versus corrected AHe age plots. Hollow markers denote aliquots considered to be outliers. The color of the markers denotes the ESR value of each aliquot. Hollow markers indicate the excluded aliquots.

Galbraith & Laslett, 1993; Green, 1981). Results are summarized in Table 1; complete AFT data are presented in Tables S1 and S4.

3.3. AHe Method

AHe thermochronology quantifies the production and accumulation of helium formed by the alpha decay of U, Th, and Sm. The temperature interval in which apatite retains helium is known as the apatite partial retention zone (APRZ), which ranges from 40°C to as high as 90°C (Farley, 2002). The AHe closure temperature is controlled by the helium retentivity of the crystal. This can be affected by the accumulated radiation damage, which is proportional to the effective uranium content (eU = U + 0.235*Th) and the time that the sample resided at temperatures below ~100°C (Flowers et al., 2009; Shuster et al., 2006). Residence within the APRZ can result in gas loss proportional to the crystal retentivity, resulting in positive correlations between eU and age. Additionally, the size and geometry of the crystals also affect helium retentivity (Brown et al., 2013; Farley et al., 1996). Internal crystal zonation and the presence of high helium or eU microinclusions can affect the age estimate (e.g., Flowers, 2009; Vermeesch et al., 2007). Detailed analytical procedures are described in Text S1. Results are summarized in Table 1; complete AHe results are presented in Table S2.

3.4. Thermal Modeling Procedures and Parameters

It is challenging to interpret thermal histories based on multiple thermochronometers due to natural dispersion and the complexities of each thermochonometer, especially when the samples are collected in different

Geochemistry, Geophysics, Geosystems

10.1029/2019GC008876

Table 1
Summary of AFT and AHe Data

Apatite fission track data														Apatite (U-Th-Sm)/He				
	Sample code	Lat. (°S)	Long. (°W)	Z (m)	N^a	Age (Ma)	±1σ (Ma)	P(χ) (%)	N^b	MTL (μm)	SD^c (μm)	Dpar (μm)	SD^d (μm)	Grain code	Age (Ma)	±1σ (Ma)	eU (ppm)	ESR (μm)^e
San Javier	16072SJ	26.9865	65.6630	605	22	65.0	4.8	99	48	11.7	1.0	2.1	0.2	A	26.0	1.8	6.9	60.2
														B	25.8	1.6	5.0	52.6
														C	60.6	1.5	9.0	62.7
														D	220.9	4.6	19.3	58.2
	16074SJ	26.7994	65.3433	929	21	89.0	4.4	94	99	11.9	1.7	2.1	0.2					
	16076SJ	26.7995	65.3570	1,232	21	101.2	4.8	97	101	11.8	1.3	2.0	0.2	A	129.3	6.7	50.7	60.1
														B	90.6	2.7	12.6	82.4
														C	83.5	3.7	26.1	54.5
														D	57.1	4.2	2.8	69.0
Tafi	16058TV	27.0813	65.6646	768	23	94.2	9.1	95				1.9	0.2	B	77.1	2.1	8.5	83.5
														C	38.9	1.3	4.1	83.6
	16060TV	27.0540	65.6696	960	21	79.5	5.1	100	51	11.5	0.9	2.0	0.1	A	36.9	2.0	6.9	70.4
														B	36.9	1.2	8.5	68.5
														C	42.5	2.8	10.6	79.6
														D	31.9	0.8	9.2	62.8
	16062TV	27.0286	65.6576	1,245	22	74.9	3.9	89				2.1	0.1	A	21.8	0.8	11.4	63.1
														B	20.1	0.6	7.5	67.7
														C	19.5	0.8	6.7	66.4
														D	34.0	1.2	13.0	59.8
	16064TV	26.9506	65.6608	1,612	22	75.5	4.5	81	52	11.9	1.3	2.1	0.2	A	15.0	0.4	7.9	78.0
														C	141.1	5.5	29.2	49.1
	16070TV	26.9506	65.6608	1818	22	94.4	4.7	81	90	13.1	1.1	2.1	0.2	A	29.5	1.6	8.7	43.4
														B	79.0	2.5	12.2	59.5
Medina	16144RN	26.4345	65.0511	1,355	21	56.7	3.5	100				1.9	0.2	A	28.5	2.4	8.9	57.9
														B	190.5	7.8	52.1	54.9
														C	67.1	2.4	11.4	49.7
	17145RN	26.4164	65.0534	1,522	20	108.0	4.6	64	61	12.0	2.0	1.8	0.1	A	53.3	5.8	10.9	44.6
														C	78.1	19.4	0.6	59.2
														D	71.2	5.6	1.6	53.9
A. Totora	16082SP	26.3804	65.5274	1,298	10	198.0	12	61				2.1	0.2	A	203.8	3.0	37.1	76.6
														B	53.3	3.8	6.6	44.4
														C	45.8	2.8	9.2	60.9
	16084CH	26.3880	65.4326	1,076	8	64.8	10.7	73				1.9	0.2	A	12.1	1.5	6.3	44.0
														B	12.3	1.2	6.5	43.8
														C	12.1	0.9	5.6	46.8
AR1	16008AN	27.5018	66.3740	1,455	20	80.0	2.8	13	76	11.8	2.0	1.9	0.2	A	55.5	5.0	17.2	45.2
														B	78.0	3.7	18.1	67.3
	16009AN	27.4925	66.3828	1,728	18	91.9	2.6	93	85	13.0	1.5	2.4	0.1	A	72.1	13.7	61.3	47.4
														B	74.7	6.9	21.9	63.0
														C	74.6	12.7	60.7	54.2
	16010AN	27.48128	66.39283	1980	19	75.1	2.2	66.4	100	12.37	1.692	1.993	0.2	A	61.2	11.8	29.8	65.7
														B	65.2	7.7	34.9	59.4
														C	62.9	7.6	31.6	89.4
	16011AN	−27.4691	−66.39283	2,259										A	67.9	5.3	41.3	75.4
														B	65.8	12.7	15.5	58.9
														C	64.2	4.9	13.8	73.5
	16012AN	27.45669	66.39592	2,496	20	71.2	2	20.71	100	12.64	1.607	2.175	0.2	B	65.3	6.6	54.3	52.6

Geochemistry, Geophysics, Geosystems

10.1029/2019GC008876

Table 1
Continued

Apatite fission track data														Apatite (U-Th-Sm)/He				
	Sample code	Lat. (°S)	Long. (°W)	Z (m)	N^a	Age (Ma)	±1σ (Ma)	P(χ) (%)	N^b	MTL (μm)	SD^c (μm)	Dpar (μm)	SD^d (μm)	Grain code	Age (Ma)	±1σ (Ma)	eU (ppm)	ESR $(\mu m)^e$
														C	67.4	2.1	96.3	54.2
														A	56.9	15.4	77.6	48.8
														B	63.5	6.0	74.2	40.2
	16013AN	−27.4446	−66.41297	2,768										C	63.0	4.5	68.7	44.2
	16014AN	−27.4204	−66.41122	2,961										A	47.0	2.2	53.0	120.6
														B	55.0	4.9	85.1	44.6
														C	51.5	2.4	91.0	41.8
AR2b	16015CP	27.3402	66.2720	4,666	16	46.7	7.7	100				1.6	0.2	E	1.4	0.1	10.7	82.5
														F	5.4	0.2	52.6	70.3
	16017CP	27.3421	66.2792	4,448	25	15.8	1.5	100				1.7	0.2	A	8.3	0.9	13.2	76.5
														B	15.7	1.3	18.4	48.1
														C	10.3	1.2	12.0	57.4
														D	5.8	0.7	6.8	64.4
	16019CP	27.3470	66.2974	4,122	20	7.0	0.8	70				1.7	0.1	A	5.0	0.8	15.7	40.2
														B	5.6	1.2	13.6	49.1
														C	6.0	1.1	11.7	42.3
														D	5.8	0.9	14.1	42.6
AR2a	16021CP	27.3601	66.3263	3,874	20	64.5	2.2	75	100	12.5	1.3	2.3	0.1	A	65.0	7.3	32.7	86.9
														B	58.4	3.1	66.5	53.4
														C	63.5	3.2	64.2	45.6
														D	50.2	6.9	53.9	64.6
														A	9.3	0.4	17.1	80.0
	16023CP	27.3531	66.3446	3,579	24	9.4	1.2	89				2.2	0.1	C	38.3	4.0	205.1	49.8
														F	6.5	1.2	9.1	40.7
														G	8.3	1.3	8.3	48.7
	16025CP	27.3460	66.3469	3,353	20	9.3	1.1	95				1.9	0.2					
	16027CP	27.3376	66.3453	3,123	22	18.4	0.9	96				2.0	0.1	B	11.2	1.6	27.5	73.4
														C	11.8	0.8	37.6	58.7
Ambato	16029AC	27.6372	66.1829	1,208	20	74.7	3.7	80				1.6	0.1					
	16031AC	27.6375	66.1720	1,517	20	95.4	3.3	68	100	13.0	1.2	2.2	0.1	A	78.8	18.0	16.6	83.4
														B	87.2	7.5	10.4	68.0
														C	83.1	12.6	13.1	69.3
	16033AC	27.6326	66.1647	1,757	20	89.9	3.4	97	101	12.5	1.4	2.1	0.1	A	92.2	9.9	40.1	64.4
														B	72.1	8.8	16.1	48.8
Guasayan	16123GY	28.1365	64.8103	524	18	125.1	4.2	23	102	11.7	1.5	2.2	0.1	B	127.1	4.5	43.2	71.5
														C	170.2	11.6	35.9	73.5
														D	155.8	6.6	33.9	72.9
														E	157.3	6.7	71.4	69.2
Candelaria	CUND02	26.28493	64.94847	1,400										B	31.5	1.6	7.5	59.4
														C	24.8	6.1	1.2	46.5
														E	29.9	7.3	0.9	41.0

Note. Only the AHe aliquots included in the thermal history models are presented in this table. Complete data tables are presented in Tables S1 and S2. Note that AHe ages are Ft corrected. ζ = 370 ± 10.8 (S.Z.) [a]Number of grains. [b]Number of measured lengths. [c]Standard deviation of measured lengths. [d]Standard deviation of measured Dpars. [e]Equivalent spherical radius.

structural positions within a transect. We performed inverse modeling with the QTQt program (v. 5.7.0), which uses a Bayesian transdimensional statistical approach to extract the most probable thermal history from robust data sets (Gallagher, 2012). In each multiple-sample model, the structurally highest and lowest samples are called the "cold sample" and the "hot sample," respectively.

AHe single grain ages that cannot be explained by the available diffusion models must be identified and excluded from the thermal history models to prevent the models from trying to fit these AHe ages. In this contribution, we have used three different criteria to choose the AHe aliquots used in the thermal history models. First, reproducible AHe single grain ages were included in the models; we consider ages to be reproducible when the 1σ S.D. is <20% of the mean age (Flowers et al., 2009; Flowers & Kelley, 2011). Second, since QTQt software utilizes helium diffusion models able to reproduce age and size controls (Gallagher, 2012), AHe single grain ages which exhibit an intrasample positive correlation between age and eU and/or size were included in the models (e.g., Flowers et al., 2007; Reiners & Farley, 2001), eU versus age plots are presented in Figure 3. Finally, elevation versus AFT and AHe ages trends were also used to identify possible AHe outliers. In all, 85 out of 105 AHe aliquots were used in the models. The criteria used for the inclusion of each aliquot are presented in Table S2.

We used the radiation damage model from Flowers et al. (2009) for AHe data and the annealing model of Ketcham et al. (2007) for AFT data. All the models were allowed to find thermal histories between 600 and 0 Ma and between 200 and 0°C to model geologically realistic radiation damage. For each model, only the time interval with a constrained solution is presented here; complete models are presented in Figure S1, and the likelihood chains are presented in Figure S2. Given that all of the samples were collected from metamorphic rocks from the Puncoviscana Fm. or from Paleozoic granitoids, a constraint to start with a reset sample between 550 and 450 Ma was added in the models. This constraint denotes the time of metamorphism of the Puncoviscana Fm. and crystallization of the metamorphic and granitoid rocks of the Puncoviscana Fm. (Ramos, 2008 and references therein). Additional stratigraphical constraints were added to each model based on the local geology. The details of these constraints and the modeling parameters are presented in Table S3.

4. Results

4.1. San Javier Range

We collected three samples from the eastern side of the San Javier Range in an ~600-m elevation profile (Figure 2b). AFT ages are between ~65 and 101 Ma with MTLs between ~11.7 and 11.8 μm. Eight single grain AHe aliquots from sample 16072SJ and 16076SJ have dispersed ages between ~26 and 220 Ma. However, since both samples exhibit positive age versus eU correlations, all aliquots were included in the model (Figures 3a and 4a). A geological constraint in the model represents the unconformity between the basement and Cretaceous strata (Figure 2). The expected thermal history model results indicate a Cretaceous (130–110 Ma) cooling event, followed by a stay at low temperatures (~50°C) until the Miocene when the section was reheated. A final fast cooling event occurred during the Pliocene (Figure 4a). This model reproduced most of the observed data. Despite the poor prediction of the older AHe aliquots, the model predicts similar age versus eU trends.

4.2. Tafi del Valle Range

We collected five samples over an ~1,000-m elevation profile in the Tafi del Valle Range (Figure 2b). AFT ages are between ~74 and 94 Ma. MTLs for samples 16060TV and 16070TV are 11.4 and 13.0 μm, respectively. Single grain AHe ages are between ~29 and 196 Ma. We modeled four reproducible AHe single grain ages from sample 16060TV; these aliquots have a mean age of ~37.0 Ma. Fourteen AHe aliquots from samples 16058TV, 16062TV, 16064TV, and 160070TV exhibit intrasample dispersion; 10 of these aliquots were modeled because they show positive correlations between age and eU (Figure 3b). The model results suggest that this block experienced cooling during the Upper Cretaceous (100–75 Ma), followed by reheating between and 75 and 40 Ma, and continuous cooling during the Miocene (Figure 4b). Our model reproduces most of the observed data. However, predicted ages for the older aliquots, which were part of the eU versus age intrasample trend, did not match the observed data.

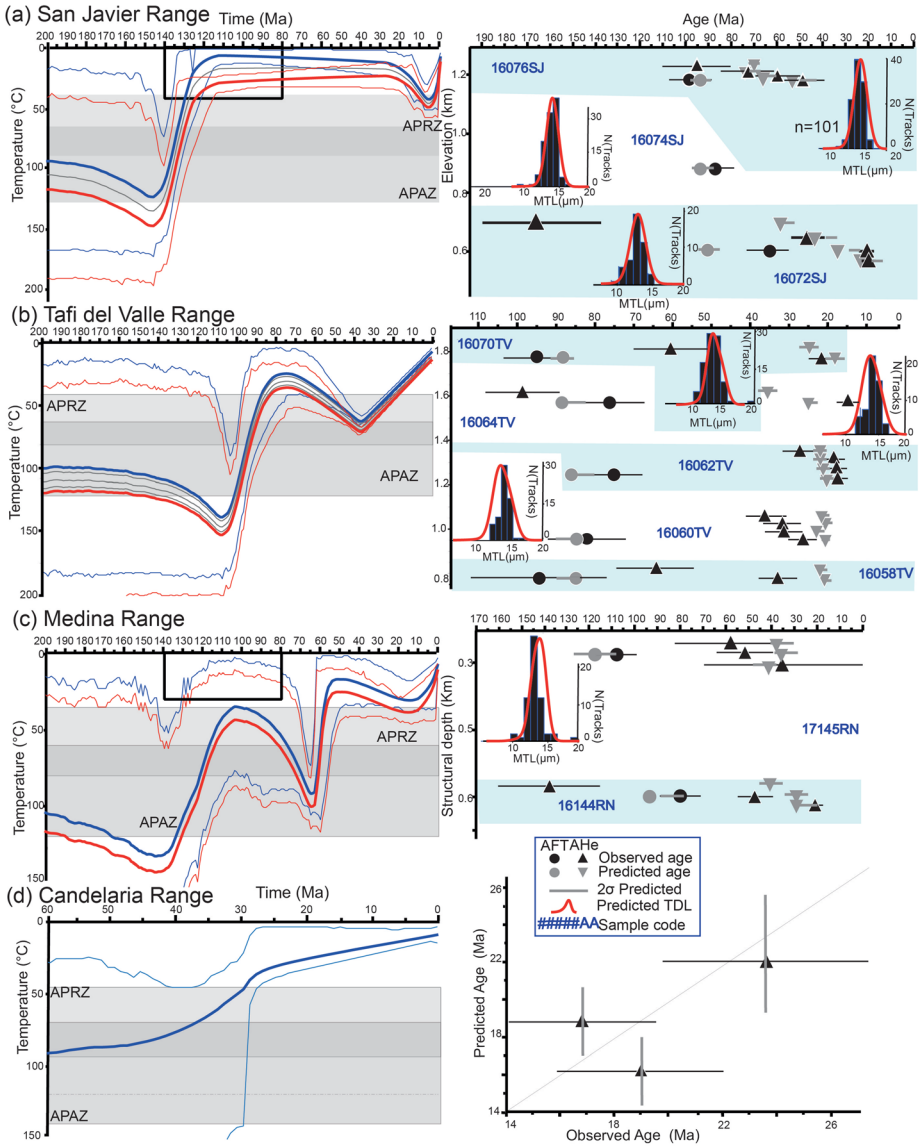

Figure 4. QTQt thermal history expected models from the (a) San Javier, (b) Tafi del Valle, (c) Medina, and (d) Candelaria ranges. Age versus elevation plots are presented for each profile, and the predicted and observed data are plotted for each model. We present the values predicted for the expected thermal history model and the 2-sigma interval of the data predicted by the post-burn-in acceptable models. The red lines denote the "hot sample" and the blue line the "cold sample" with their respective 95% confidence intervals. Black boxes indicate the model constraints. For a sample with several AHe ages, a small elevation perturbation was added to the plot to facilitate data visualization. Shaded blue areas are used to group the AFT and AHe data from the same sample. TLD are presented for each sample; red lines denote the predicted TLD.

4.3. Medina and Candelaria Ranges

We collected basement samples 17145RN and 16144RN at 0.2- and 0.7-km distance from the unconformity on the western side of the Medina Range (Figure 2). Sample 17145RN has an AFT age of ~108 Ma with a MTL of ~12.0 μm and AHe single grain ages between ~40 and 78 Ma. We modeled three reproducible aliquots with a mean age of ~67.5 Ma. Sample 16144RN has an AFT age of ~65 Ma and dispersed AHe single grain ages between ~28 and 190 Ma. Three of these aliquots were included in the model because they exhibit a positive correlation between age and eU. We added a constraint to the model to represent the unconformity between the basement and Cretaceous strata. The structural depth with respect to the unconformity was incorporated in the model. The expected model results suggest a Cretaceous cooling event between 130

and 100 Ma followed by reheating between 80 and 65 Ma (Figure 4c). After reheating, the model suggests cooling between 60 and 50 Ma. During the Neogene, the model suggests slow reheating and cooling after 10 Ma. The model successfully predicted most of the observed data except for the oldest aliquot from sample 16144RN.

One sample from the metamorphic basement of the Candelaria Range exhibits AHe grain ages between ~25 and 62 Ma (Figure 3c). We modeled three reproducible AHe aliquots with a mean age of ~28.7 Ma. The model suggests cooling below 50°C at ~30 Ma (Figure 4d). The model reproduces the ages of the three AHe ages.

4.4. Capillitas and Aconquija Ranges

We collected 14 basement samples between 1,000 and 4,600 masl along two different elevation profiles in the Capillitas and Aconquija ranges. We collected seven basement samples between 1,000 and 2,500 masl in profile AR1, which is located in the Capillitas Range. In profile AR2, we collected eight basement samples between 2,500 and 4,600 masl at the southern end of the Aconquija Range (Figure 1b). Profile AR2 crosses the Agua Rica Fault; therefore, we divided this profile into AR2a in the footwall and AR2b in the hanging wall (Figure 2b).

The transect AR1 exhibits Cretaceous AFT ages (~70–90 Ma) with shortened MTLs (~11.8–13.0 μm) and 19 AHe single grain ages between ~51 and 78 Ma. Since all the samples exhibit intrasample reproducible AHe ages, all of the aliquots were included in the model (Figure 3d). The expected thermal history model suggests Cretaceous cooling between ~90 and 85 Ma followed by reheating between ~75 and 65 Ma and then cooling between 60 and 55 Ma. During the Neogene, the model suggests slow reheating up to ~50°C and cooling after 10 Ma (Figure 5c). This model successfully reproduces most of the observed data.

The lower three samples (16023CP, 16025CP, and 16027CP) from the segment AR2a have AFT ages between ~9.3 and 18.4 Ma. The highest sample (16021CP) has an AFT age of 64.5 Ma and MTL of 12.5 μm. We modeled two reproducible aliquots with a mean age of ~11.5 Ma from sample 16027CP (Figure 3e). Three aliquots from sample 16023CP were included because they exhibit a positive correlation between AHe age and eU. We excluded AHe aliquots from samples 16025CP because, despite having similar low eU values (<10 ppm), these aliquots have older ages than the reproducible AHe ages from the samples immediately above and below. Moreover, these AHe ages are older than the AFT ages from the profile (Figures 3e and 3f). We modeled four reproducible aliquots with a mean age of ~59.2 Ma from sample 16021CP. The AR2a expected model shows rapid Late Cretaceous cooling, followed by Late Miocene reheating within the APAZ, ending with rapid cooling around 10 Ma (Figure 5b). The model succeeds at reproducing the data including the observed AHe age versus eU trend in sample 16023CP. Although sample 16021CP has four reproducible AHe ages, the model predicts a size versus age trend for this sample. Older ages were predicted for the two aliquots with higher eU values (Figure 5b).

The three samples from profile AR2b have AFT ages between 7.0 and 15.8 Ma for the lower samples (16017CP and 16019CP) and ~46.7 Ma for the highest sample (16015CP). Single grain AHe ages from the lower samples are between 5.0 and 15.7 Ma. The highest sample (16015CP) has AHe single grain ages between 1.4 and 20.8 Ma. We modeled data from three reproducible AHe aliquots with a mean age of ~5.6 Ma from sample 16019CP. We modeled four aliquots from sample 16017CP and two from sample 16015CP because they exhibit positive intrasample correlations between AHe age and eU (Figure 3f). The AR2b model shows Miocene reheating and fast exhumation at ~5 Ma. This model successfully reproduces most of the data except for the AHe age versus eU trend observed in sample 16017CP.

Despite the presence of Miocene volcanic deposits (12–4 Ma) close to the collected samples, unreset samples (e.g., 16021CP) suggest that the measured ages were not significantly affected by magmatism. Additionally, fully reset AFT and AHe (~10 Ma) ages are older than the reported ages for the nearby Miocene intrusives (~6 Ma) (Landtwing et al., 2002). The lack of Miocene magmatic resetting could be related to shallow emplacement depths and volumetrically small intrusives (Murray et al., 2018).

4.5. Altos del Totora Range

We collected two samples in the Altos de la Totora range (Figure 2b). Sample 16082SP was collected from basement on the western flank of the range, below Paleogene strata. Sample 16084CH was collected

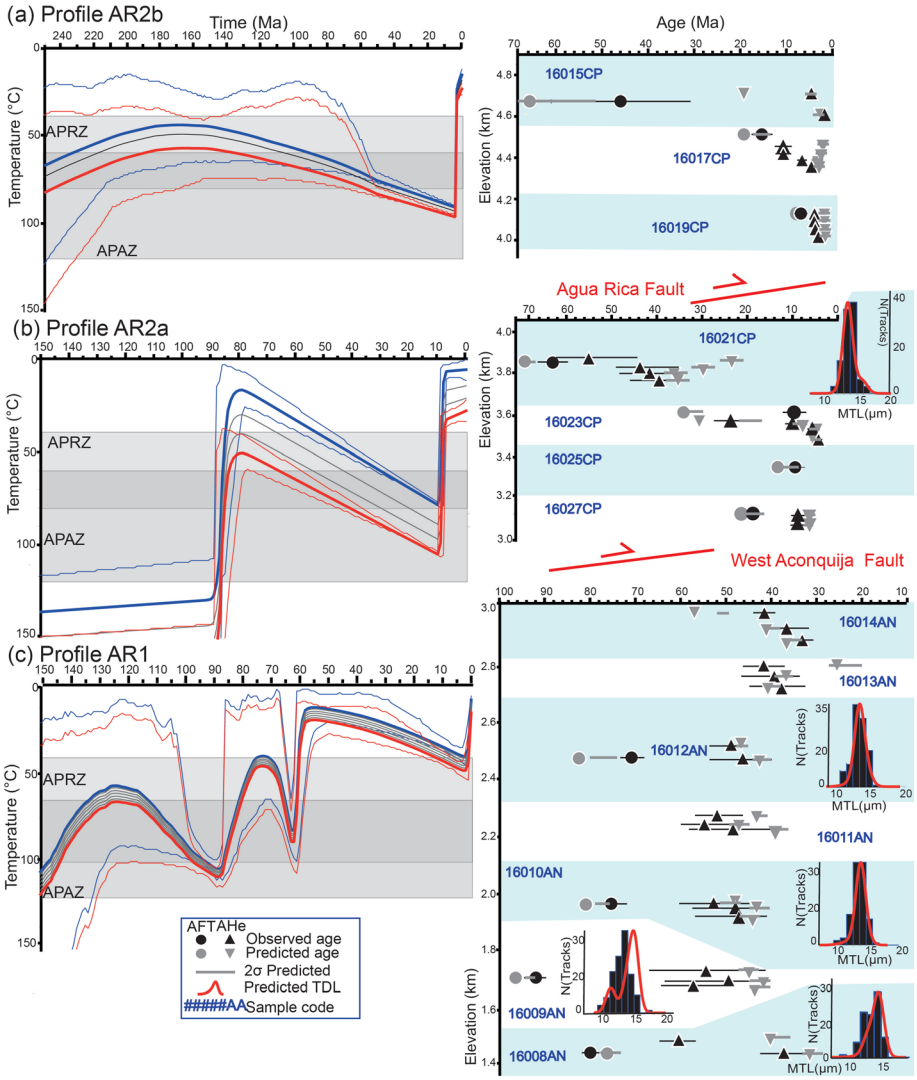

Figure 5. (a–c) Thermal history expected models from the Capillitas and the Aconquija ranges. See Figure 4 for the detailed caption.

~9 km east of the discordance close to the Altos del Totora Fault (Figure 2b). Sample 16082SP has an AFT age of ~198 Ma and dispersed AHe single grain ages between 45.8 and 203.8 Ma; three of these aliquots were modeled because they exhibit a positive correlation of age with eU and grain size (Figure 3g). Sample 16084CH has an AFT age of ~64 Ma and three reproducible AHe aliquots with a mean age of ~12 Ma; these aliquots were modeled (Figure 3g). We added a constraint to the model to represent the unconformity between the basement and the Paleogene sedimentary rocks. We incorporated the structural depth with respect to the unconformity (Figure 7a). The multiple-sample model shows a long residence of the cold sample at temperatures below 50°C followed by reheating between 75 and 65 Ma. Cold and hot samples exhibit a cooling event between 50 and 40 Ma. Paleogene cooling was followed by slow cooling for the cold sample and continuous cooling for the hot sample. The absence of Miocene cooling in the cold sample thermal history can be explained by the sample residing in a shallow position above the APRZ prior to the Miocene exhumation (Figure 6a). The model reproduces all the observed data including the AHe age versus eU trend observed in sample 16082SP.

4.6. Ambato Range

We collected three samples on the western side of the range in an ~500-m elevation profile (Figure 2b). The samples were collected below a continuous east-dipping paleosurface on the eastern flank of the range

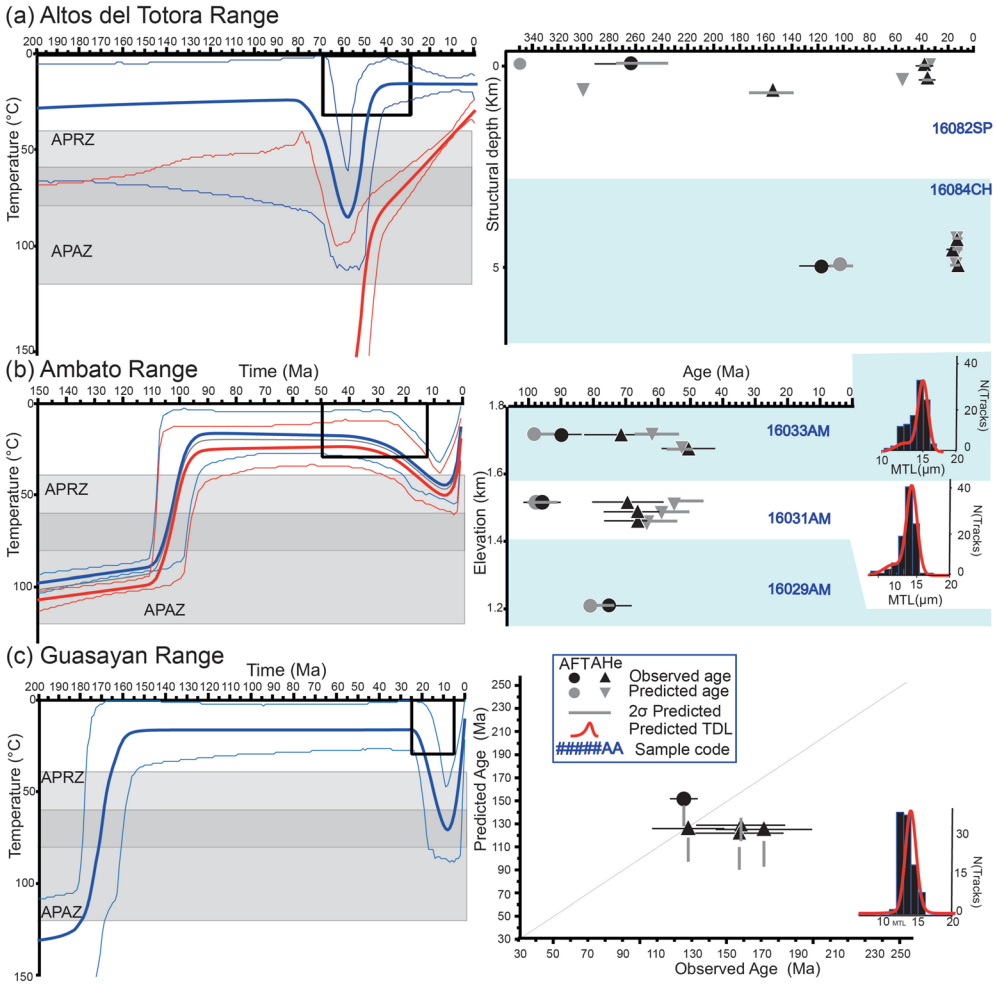

Figure 6. Thermal history expected models from the (a) Altos del Totora, (b) Ambato, and (c) Guasayan ranges. See Figure 4 for a detailed caption.

(Figure 2b). AFT ages are between ~75 and 95 Ma; samples 16033AM and 16029AM have MTLs of ~12.5 and 13.0 μm, respectively. We modeled six aliquots from samples 16033AM and 16031AM because they have intrasample reproducible AHe ages with mean ages of ~82.1 and ~83.1 Ma, respectively (Figure 3h). Since Miocene strata overlie this paleosurface farther north, we added a stratigraphic constraint to represent this unconformity in the model. The expected thermal history model suggests Late Cretaceous exhumation (110–90 Ma) followed by a stay at low temperatures (~50°C) until the Miocene when the section was reheated. A final fast cooling event took place during the Pliocene (Figure 6b). The model reproduces the observed data.

4.7. Guasayan Range

On the western side of the range (Figure 2b), we collected one sample with an AFT age of ~125 Ma and an MTL of ~11.7 μm. Single grain AHe ages are between ~127 and 170 Ma. We modeled data from four reproducible aliquots with a mean age of ~152 Ma (Figure 3h). We added a stratigraphic constraint to the model to represent the unconformity between crystalline basement and Late Miocene sedimentary rocks. The single-sample model suggests a fast cooling event around 160 Ma followed by ~80 Ma of residence at temperatures below 40°C, followed by Miocene reheating and exhumation (Figure 6c). This model poorly fits three of the AHe ages. However, the long residence at low temperatures followed by Miocene reheating predicts the observed overlap between AFT and AHe ages and the shortened TLD.

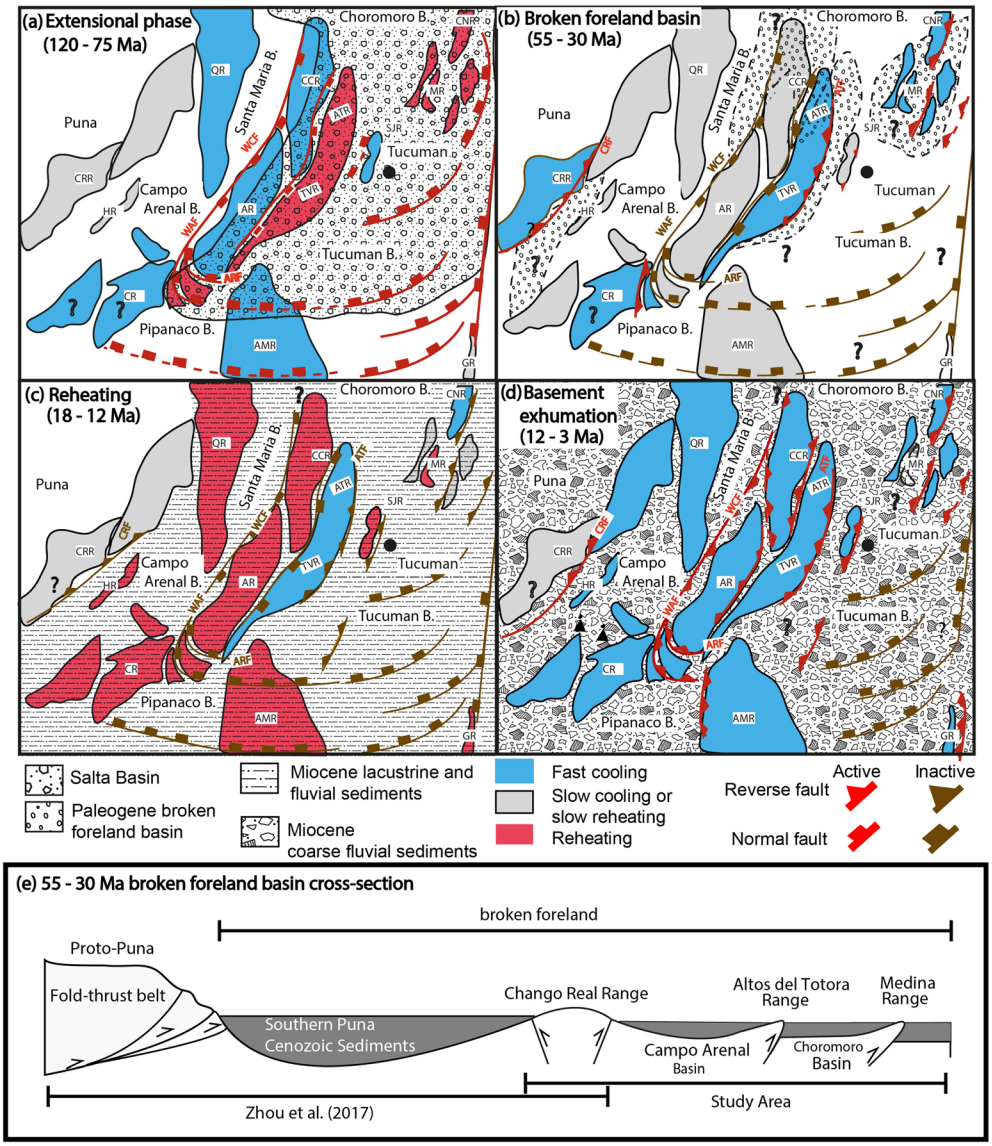

Figure 7. (a–d) Schematic evolution of the study area, highlighting the periods of cooling and reheating of the basement and the interpreted fault activity through time. The city of Tucuman is shown as a reference point. ATR: Altos de la Totora Range, CCR: Cumbres Calchaquies Range, MR: Medina Range, SJR: San Javier Range, CNR: Candelaria Range, HR: Cuevas-Hualfin Range, CR: Capillitas Range, AR: Aconquija Range, TVR: Tafi del Valle Range, AMR: Ambato Range, GR: Guasayan Range, WCF: West Cumbres Calchaquies Fault; WAF: West Aconquija Fault; EAF: East Aconquija Fault, ATF: Altos de la Tortora Fault. (e) Cross section of the Paleogene broken foreland.

5. Discussion

5.1. Structure of the Southern End of the Salta Basin (120–75 Ma)

Published thermochronologic data and our models from the study area suggest that Cretaceous (120–75 Ma) exhumation occurred in several of the studied blocks (Carrapa et al., 2014; Löbens et al., 2013; Mortimer et al., 2007). This exhumation event was coeval with the deposition of syn-rift strata in the Choromoro and Tucuman Basins and farther north in the Salta Basin (130–80 Ma) (Iaffa et al., 2013; Marquillas et al., 2005; Porto et al., 1982). The Guasayan Range has an older modeled exhumation age of ~160 Ma (Figure 7c). Similar Jurassic exhumation has been documented in the Hualfin Range in the Campo-Arenal Basin (Zapata et al., 2019b); this Jurassic cooling event could reflect extensional phases before the development of the Salta Basin (Bense et al., 2013; Schmidt et al., 1995).

Thermochronologic data from the San Javier, Cumbres Calchaquies, Quilmes, and Hualfin Ranges show extensive Cretaceous cooling without subsequent Cretaceous reheating (Löbens et al., 2013; Mortimer et al., 2007; Sobel & Strecker, 2003). After the Cretaceous cooling, the Aconquija Range experienced continuous reheating until the Miocene (Figures 5a and 5b). In contrast, inverse thermal models for the Capillitas, Tafi del Valle, Altos del Totora, and Medina Ranges exhibit Late Cretaceous cooling between 130 and 70 Ma, quickly followed by Late Cretaceous to Eocene reheating (80–55 Ma). This cooling of basement blocks in the HSP and the Santa Barbara system can be related to footwall exhumation along Cretaceous normal faults (Cristallini et al., 1997; Iaffa et al., 2011; Löbens et al., 2013). We interpret the reheating in the Santa Barbara system and the Aconquija Range to be a consequence of sedimentary burial during the infilling of rift-related depocenters (Figure 7a).

Exhumation in the Aconquija and Cumbres Calchaquies Ranges removed the stratigraphic evidence of a relationship between the southeast-dipping faults located to the west of the Aconquija and Cumbres Calchaquies Ranges (WAF and WCF) and the potential Cretaceous sedimentary fill. However, seismic reflection data suggests that Cretaceous strata was not deposited west of these faults (Figure 2) (Bossi & Muruaga, 2009). Moreover, contrary to the thermal histories of the basement blocks to the west of the WAF and WCF, most blocks in the Santa Barbara system exhibit Cretaceous reheating. These differences in reheating can be used to reconstruct the extent of the Cretaceous sedimentary fill. Thus, it is plausible that these high-angle east-dipping faults acted as normal structures during the Cretaceous and controlled the extent of the Salta Basin sedimentary fill (Figure 7a).

Seismic reflection data document a change in the dominant strike of the Cretaceous normal faults from NNE in the Choromoro Basin to ENE in the Tucuman Basin (Figure 7a) (Iaffa et al., 2011, 2013). West of the Tucuman Basin, the ~NE striking reverse West Aconquija Fault splits into several NW-striking structures oriented perpendicular to the trend of the range (Figure 1b). Despite the lack of direct information about the relationship between these faults and the Cretaceous sedimentary fill, the change in the dominant strike of the West Aconquija Fault coincides with the changes in the strike of the Cretaceous normal faults preserved in the Tucuman Basin. Therefore, we suggest that the geometry of the West Aconquija Fault may resemble the geometry of the former Cretaceous rift basin. South of these ~NW- and ENE-striking normal structures, the Ambato Range experienced Late Cretaceous exhumation without subsequent reheating. The Upper Cretaceous exhumation of the Ambato Range, the change in the geometry of the reverse faults, and the absence of syn-rift deposits or Cretaceous reheating south of the Tucuman Basin suggest that these NW- and ENE-striking normal faults were part of a horst block which defined the southern structural limit of the Salta Basin (Figure 7a).

The different strikes of the Cretaceous normal faults in the study area could be the result of consecutive multiple noncoaxial extensional phases and/or preexisting structures controlling the strike of the normal faults (e.g., Grier et al., 1991; Morley et al., 2004). Late Cretaceous horst exhumation in most of the studied basement blocks suggests that faults with contrasting strike orientations were active during the same extensional event. Thus, a plausible explanation is that pre-Mesozoic basement structures controlled the rift geometry. Similar changes in the architecture of normal faults due to preexisting structures have been documented farther north in the Salta Basin and farther south in the Sierras Chicas Basin (Grier et al., 1991; Kley & Monaldi, 2002; Schmidt et al., 1995).

5.2. A Paleogene Broken Foreland (55–30 Ma)

We have robustly modeled cooling that occurred between 60 and 30 Ma. On the western flank of the Choromoro Basin, cooling is documented in the Tafi del Valle and Altos del Totora Ranges, which are bounded by the Rearte Fault to the west and the Altos del Totora Fault to the east (Figure 2). The Paleogene exhumation of this block continued toward the south, on the eastern flank of the Aconquija Range, as suggested by ~58 Ma AHe ages (Löbens et al., 2013). Cooling in the Capillitas Range initiated between 60 and 50 Ma (Figure 5c). In the eastern Choromoro Basin, the thermal history model of the Medina Range exhibits cooling between 60 and 50 Ma (Figure 4c). Moreover, the thermal history model of the Candelaria Range suggests final cooling at ~30 Ma (Figure S2). Detrital AFT data from the El Cajon Basin also suggest that exhumation in the source area occurred between 58 and 30 Ma (Mortimer et al., 2007). West of the Campo-Arenal Basin, the Chango Real Range yielded AFT ages between ~40 and 30 Ma, interpreted to reflect Eocene exhumation (Coutand et al., 2001).

Paleogene cooling was restricted to the Medina, Candelaria, Tafi del Valle, Altos del Totora, Capillitas, and Chango Real Ranges. During the same time interval, interspersed basement blocks, such as the Quilmes, San Javier, Hualfin, Ambato, Cumbres Calchaquies, and Guasayan Ranges, did not experience fast cooling or reheating (Löbens et al., 2013; Mortimer et al., 2007; Zapata et al., 2019b). These relative quiescent thermal histories combined with the paleosurfaces developed on top of these basement blocks suggest that these blocks had low relief during the Paleogene (Zapata et al., 2019b). We consider that the development of a broken foreland basin can explain the documented exhumation pattern, in which disconnected blocks with fast cooling were interspersed with blocks with quiescent thermal histories (Figures 7d and 7e).

Alternative scenarios to explain this cooling pattern, such as forebulge erosion or regional thermal cooling would require a homogeneous north-south cooling pattern along the studied area; this is not observed. Moreover, regional thermal subsidence in this area commenced around 70 Ma (Marquillas et al., 2005), before the documented Paleogene cooling. Additionally, these disconnected basement blocks are separated by reverse faults that were active during the Cenozoic (Abascal, 2005; Iaffa et al., 2013; Löbens et al., 2013) (Figure 1b).

The thermal history models from the Medina and Capillitas Ranges show cooling between ~60 and 55 Ma. However, stratigraphy and geological mapping show that the Salta rift was characterized by the deposition of post-rift strata of the Santa Barbara subgroup between ~70 and 58 Ma (Hyland et al., 2015; Marquillas et al., 2005). Since these units were deposited on top of some of these blocks (Figure 2) (Bossi, 1969; Iaffa et al., 2013), we suggest that the development of thick-skin deformation started at ~55 Ma, at the younger limit of the modeled cooling intervals (Figure 7b).

During the Eocene–Oligocene, thick-skin deformation in the study area was restricted to the HSP and the Santa Barbara system. The deformation front advanced to the Choromoro Basin in the Santa Barbara system and the eastern flank of the Aconquija Range in the HSP during this interval. Late Miocene to Pliocene exhumation of the Ambato and the Guasayan Ranges marks the development of the LSP broken foreland. Therefore, the broken foreland basin in the Santa Barbara system is older than the broken foreland basin in the LSP.

5.3. Neogene Reheating and Basin Fragmentation (18–3 Ma)

During the Miocene, the Ambato, San Javier, Medina, Hualfin, Guasayan, Cumbres Calchaquies, Quilmes, and Aconquija blocks experienced a reheating peak within the APRZ and the APAZ (Löbens et al., 2013; Mortimer et al., 2007; Sobel & Strecker, 2003). We interpret this reheating to be related to the deposition of 1.5 to 3 km of Miocene (18–13 Ma) strata on top of the crystalline basement (Figure 7c) (Zapata, et al., 2019a). The Altos del Totora, Candelaria, and Tafi de Valle Ranges, which were exhumed during the Paleogene, did not experience Miocene reheating and instead continued cooling. Other blocks that cooled between 55 and 30 Ma, such as the Medina and the Capillitas Ranges, experienced minimal amounts of Miocene reheating in which the structurally deepest, hot sample briefly resided at the upper limit of the APRZ (~40°C). A plausible explanation for differential Miocene reheating is that the blocks which were exhumed during the Paleogene experienced more rock uplift than the basement blocks which were not exhumed. Therefore, since these basement blocks were at different positions with respect to basin base level, they were overlain by different thicknesses of Miocene strata, which caused differential reheating.

During the Late Miocene and Pliocene, approximately E-W compression characterized the Central Andes (Chen et al., 2019; Kley et al., 2005). Our model results (Figure 5) indicate that cooling of the Aconquija Range started in the south at ~12 Ma with the inversion of normal faults in the southwestern part of the former Salta Basin. The sedimentary strata in the Pipanaco Basin is correlatable with the units described in the Campo-Arenal Basin (Davila et al., 2012). Since the top of crystalline basement in the Pipanaco Basin is located ~2 km below sea level, at least ~7 km of differential rock uplift was accommodated during the Middle Miocene along the southern flank of the Acoquija Range. The thermal models suggest thermal offsets of ~65°C and 25°C across the West Aconquija and Agua Rica Faults, respectively. Considering geothermal gradients between 25 and 50°C/km, these two faults accommodated between ~1.8 and 3.6 km of relative rock uplift. One or more reverse faults farther south in the Pipanaco Basin and the Capillitas Range may have accommodated the remaining rock uplift. The reactivation of normal faults on the SW flank of the Aconquija Range also limited the along-strike development of this orographic

barrier and compartmentalized the Campo-Arenal Basin. The faults in the southern end of the Aconquija Range have been interpreted as strike-slip faults (Seggiaro et al., 2014). However, we have documented significant vertical rock uplift along these faults. These findings do not necessarily negate the previous interpretation because thermochronological data cannot constrain the strike-slip component of motion.

Published AFT and AHe ages from the northern part of the Aconquija Range are between ~8 and 3 Ma; the ages from the humid side are the youngest (~3 Ma) (Löbens et al., 2013; Sobel et al., 2003). The aridification of the Campo-Arenal Basin at ~3 Ma reflects the development of a rain shadow driven by topographic growth of the Aconquija Range (Sobel & Strecker, 2003). We suggest that the cooling offset documented along the Agua Rica and the West Aconquija Faults may have been responsible for the initial surface uplift of the southern part of the Aconquija Range after ~12 Ma. Subsequently, the development of an orographic barrier focused precipitation and hence enhanced erosion on the central humid side of the range. Similar orographic precipitation controls on the amount of exhumation have been documented in ranges such as the Himalayas (e.g., Adlakha et al., 2013; Thiede et al., 2004).

The amount of cooling experienced by the Aconquija Range was at least 100°C higher than in the surrounding ranges, especially the Cumbres Calchaquies Range, located along-strike toward the north (Figure 1b). Thus, considering geothermal gradients between 25 and 50°C/km, the Aconquija Range experienced 2 to 4 km more exhumation than the Cumbres Calchaquies Range during the Miocene–Pliocene (Löbens et al., 2013; Sobel et al., 2003). Structural models have shown that the number of reverse faults accommodating Miocene shortening is larger in the north (HSP and Santa Barbara system) than in the south (LSP) (Figure 7d) (Abascal, 2005; Cristallini et al., 2004; Iaffa et al., 2013). Furthermore, in the LSP, the strike of the Cretaceous faults is subparallel to the maximum compression direction. Therefore, it is plausible that this angular relationship hindered basin inversion and the propagation of deformation toward the Tucuman Basin (Iaffa et al., 2011). As a consequence, shortening was mostly accommodated in the Aconquija Range, leading to a higher amount of basement exhumation. In the Santa Barbara system and the HSP, the ~NE strike of the normal faults promoted the exhumation of several basement blocks. Therefore, shortening was distributed among more faults, which may have caused less basement exhumation in the northern ranges compared to the Aconquija Range.

5.4. Upper Plate Controls on the Development of Broken Foreland Basins and Implications for Andean Tectonic Models

The LSP broken foreland transitions toward the north into the Santa Barbara system and the Puna Plateau. This transition coincides with the southern limit of the Salta Basin, documented in this contribution. Therefore, we suggest that upper plate pre-Miocene structures were the main precursor of the along-strike segmentation observed in the study area. Herein, we show that the along-strike segmentation of this portion of the Andes predates Late Oligocene to Miocene flat-slab subduction (26 Ma, Gianni et al., 2020) and controlled the subsequent deformation style. These conclusions imply that Late Oligocene–Miocene slab flattening was not responsible for the along-strike segmentation and the deformation patterns of the northern limit of the Sierras Pampeanas.

Several tectonic models proposed the existence of a continuous Paleogene foreland basin associated with a topographic load farther west (Carrapa et al., 2008; Ramos et al., 2002; Ramos & Folguera, 2009; Zhou et al., 2017). Conversely, the model presented herein documents the development of an Eocene to Oligocene broken foreland basin in the Andean retroarc (Figure 7e). Between 55 and 30 Ma, at ~27°S thick-skin deformation was distributed among several deformational fronts, including the proto-Puna Plateau (Zhou et al., 2017), the Chango Real Range (Coutand et al., 2006), the Altos del Totora Range, and the Eastern Ranges (this contribution) (Figure 7e). This deformational pattern implies that during the Eocene deformation migrated from the Western Cordillera (Arriagada et al., 2006; Kraemer et al., 1999; Zhou et al., 2017) into the Andean retroarc, encompassing a segment of an ~500 km wide deformation zone. Coeval deformation along several disconnected deformational fronts cannot be explained by the advance of a single orogenic wedge into the foreland basin (DeCelles & Giles, 1996; Martinod et al., 2020). Tectonic models proposed for other segments of the Andes suggest that migration of deformation into the Andean retroarc was promoted by flat-slab subduction (e.g., Horton, 2018b; Martinod et al., 2020). Farther north in the Central Andes (~22–24°S), Eocene to Oligocene retroact deformation was coeval with a period of flat-slab subduction (Haschke et al., 2002; Horton, 2018b; Martinod et al., 2020). However, between 26°S and 28°S,

the Eocene to Oligocene magmatic arc remained on the Western Cordillera, suggesting Paleogene normal subduction in this segment of the Central Andes (Gianni et al., 2020). Therefore, in our study area, flat-slab subduction was not the main precursor of the documented eastward migration of deformation during the Eocene.

Slab reconstructions have shown that the penetration of the slab into the lower mantle promoted compressional tectonics in the Central Andes (Chen et al., 2019; Faccenna et al., 2017). Numerical models predict retroarc compression once the slab is anchored (Faccenna et al., 2017). Between 26°S and 28°S, slab anchoring in the study area occurred between ~54 and 44 Ma (Chen et al., 2019). Since in our study area, the documented thick-skin deformation partially coincides with a period of slab anchoring and steep subduction, we suggest that the documented deformation in the Andean retroarc could result from upper plate compression promoted by slab anchoring.

Our findings suggest that deformation can take place ~700 km from the trench during a period of steep subduction. Thus, flat subduction was not necessary to shift deformation toward the foreland or to form broken foreland basins. Although initial deformation and formation of a broken foreland were not linked to flat-slab subduction, the Miocene reactivation of these structures may have been aided by slab flattening. Previous work linking flat-slab subduction with the formation of Miocene broken foreland systems in the Sierras Pampeanas (Carrapa et al., 2008; Encinas et al., 2016; Jordan et al., 1983; Ramos & Folguera, 2009) lacked information about the Paleogene foreland evolution. While Eocene to Oligocene retroarc compression was related to slab anchoring, the upper plate inherited structures hindered or facilitated the migration of deformation, controlling deformation patterns, the amount of exhumation, and geometry of the foreland. These findings are critical for the interpretation of the sedimentation and deformation patterns of foreland basins.

6. Conclusions

We have documented the thermal histories of nine basement blocks between 26°S and 28°S. During the Cretaceous, horst uplift and the development of the Salta rift depocenters caused exhumation and reheating of the basement. Between 55 and 30 Ma, several disconnected basement blocks were deformed and exhumed as part of a broken foreland basin. During the early Miocene, burial beneath more than 2 km of sediments caused reheating of several basement blocks. This contribution documents the controls exerted by preexisting basement structures on basin geometry, the amount of basement exhumation, and deformation patterns during the Cenozoic deformation phases. Our model suggests that the observed segmentation of the Andean retroarc was controlled by preexisting basement structures, prior to Miocene slab flattening. Therefore, flat-slab subduction is not necessary to create a broken foreland. The development of a broken foreland during the Eocene–Oligocene argues against previous models that propose the existence of a continuous undeformed foreland basin. In this region, Paleogene compression may have been caused by slab anchoring while upper plate structures controlled the development of the studied broken foreland basins and the along-strike segmentation of the Andean retroarc.

Acknowledgments

We acknowledge the Deutsche Forschungsgemeinschaft (DFG, Grant STR373/34-1) and the Brandenburg Ministry of Sciences, Research and Cultural Affairs, Germany, for funding this study as part of the International Research Training Group IGK2018(StRATEGy). We also acknowledge the German-Argentine University Network (DAHZ/CUAA), the Argentinean science foundation (CONICET), and CICTERRA for their funding and support. We would especially like to thank M. Strecker for helpful discussions, G. Aranda and P. Payrola for assistance with samples, and A. Bergner, H. Wichura, V. Torres, and A. Gutierrez for their administrative support. The reviewers Brian K. Horton and David M. Pearson are acknowledged for their constructive comments.

Data Availability Statement

All the data used in this manuscript can be found in the supporting information. All of the data have been archived at the geochron database (https://www.geochron.org/dataset/html/geochron_dataset_2019_10_24_c17eU).

References

Abascal, L. D. V. (2005). Combined thin-skinned and thick-skinned deformation in the central Andean foreland of northwestern Argentina. *Journal of South American Earth Sciensssces*, *19*(1 SPEC. ISS), 75–81. https://doi.org/10.1016/j.jsames.2005.01.004

Adams, C. J., Miller, H., & Toselli, A. J. (2007). Detrital zircon ages of the Puncoviscana Formation of NW Argentina, and their bearing on stratigraphic age and provenance. In *20th Colloquium on Latin American Earth Sciences, Kiel* (pp. 68–69). Stuttgart, Germany: E. Schweizerbart'sche Verlagsbuchhandlung.

Adams, C. J., Miller, H., Toselli, A. J., & Griffin, W. L. (2008). The Puncoviscana Formation of Northwest Argentina: U-Pb geochronology of detrital zircons and Rb-Sr metamorphic ages and their bearing on its stratigraphic age, sediment provenance and tectonic setting. *Neues Jahrbuch Fur Geologie Und Palaontologie - Abhandlungen*, *247*(3), 341–352. https://doi.org/10.1127/0077-7749/2008/0247-0341

Adlakha, V., Lang, K. A., Patel, R. C., Lal, N., & Huntington, K. W. (2013). Rapid long-term erosion in the rain shadow of the Shillong Plateau, Eastern Himalaya. *Tectonophysics*, *582*, 76–83. https://doi.org/10.1016/j.tecto.2012.09.022

Arriagada, C., Cobbold, P. R., & Roperch, P. (2006). Salar de Atacama basin: A record of compressional tectonics in the Central Andes since the mid-Cretaceous. *Tectonics*, *25*, TC1008. https://doi.org/10.1029/2004TC001770

Becker, T. P., Summa, L. L., Ducea, M., & Karner, G. D. (2015). Temporal growth of the Puna Plateau and its bearing on the post-Salta rift system subsidence of the Andes foreland basin at 25 30′S. In *Geodynamics of a Cordilleran Orogenic System: The Central Andes of Argentina and Northern Chile. Geological* (pp. 407–433). Washington, DC: The Geological Society of America.

Bense, F. A., Löbens, S., Dunkl, I., Wemmer, K., & Siegesmund, S. (2013). Is the exhumation of the Sierras Pampeanas only related to Neogene flat-slab subduction? Implications from a multi-thermochronological approach. *Journal of South American Earth Sciences*, *48*, 123–144. https://doi.org/10.1016/j.jsames.2013.09.002

Bossi, G. E. (1969). *Geología y estratigrafía del sector sur del Valle de Choromoro*. San Miguel de Tucumán, Argentina: Universidad Nacional de Tucumán, Fundación e Instituto Miguel Lillo.

Bossi, G. E., & Muruaga, C. M. (2009). Estratigrafía inversión tectonica del "rift" Neogeno en el Campo del Arenal, Catamarca, NO Argentina. *Andean Geology*, *36*(2), 311–341. https://doi.org/10.4067/S0718-71062009000200007

Brown, R. W., Beucher, R., Roper, S., Persano, C., Stuart, F., & Fitzgerald, P. (2013). Natural age dispersion arising from the analysis of broken crystals. Part I: Theoretical basis and implications for the apatite (U-Th)/He thermochronometer. *Geochimica et Cosmochimica Acta*, *122*(120), 478–497. https://doi.org/10.1016/j.gca.2013.05.041

Canavan, R. R., Carrapa, B., Clementz, M. T., Quade, J., Decelles, P. G., & Lindsay, M. (2014). Early Cenozoic uplift of the Puna Plateau, Central Andes, based on stable isotope paleoaltimetry of hydrated volcanic glass. *Geology*, *42*(5), 447–450. https://doi.org/10.1130/G35239.1

Carlson, W. D., Donelick, R. A., & Ketcham, R. A. (1999). Variability of apatite fission-track annealing kinetics: I. Experimental results. *American Mineralogist*, *84*(9), 1213–1223. https://doi.org/10.2138/am-1999-0901

Carrapa, B., Bywater-Reyes, S., Safipour, R., Sobel, E. R., Schoenbohm, L. M., DeCelles, P. G., et al. (2014). Errata to The effect of inherited paleotopography on exhumation of the Central Andes of NW Argentina [Geological Society of America, 126, 1/2, 66-77]. *Bulletin of the Geological Society of America*, *126*(3–4), 615. https://doi.org/10.1130/B30844.1

Carrapa, B., Hauer, J., Schoenbohm, L., Strecker, M. R., Schmitt, A. K., Villanueva, A., & Sosa Gomez, J. (2008). Dynamics of deformation and sedimentation in the northern Sierras, Pampeanas: An integrated study of the Neogene Fiambalá basin, NW Argentina. *Bulletin of the Geological Society of America*, *120*(11–12), 1518–1543. https://doi.org/10.1130/B26111.1

Chen, Y. -W. W., Wu, J., & Suppe, J. (2019). Southward propagation of Nazca subduction along the Andes. *Nature*, *565*(7740), 441–447. https://doi.org/10.1038/s41586-018-0860-1

Coughlin, T. J., O'Sullivan, P. B., Kohn, B. P., & Holcombe, R. J. (1999). Apatite fission track thermochronology of Sierras Pampeanas central western Argentina: Implications for the mechanism of plateau-uplift in the Andes. *Geology*, *26*(11), 999–1002. https://doi.org/10.1130/0091-7613(1998)026<0999:AFTTOT>2.3.CO;2

Coutand, I., Carrapa, B., Deeken, A., Schmitt, A. K., Sobel, E. R., & Strecker, M. R. (2006). Propagation of orographic barriers along an active range front: Insights from sandstone petrography and detrital apatite fission-track thermochronology in the intramontane Angastaco basin, NW Argentina. *Basin Research*, *18*(1), 1–26. https://doi.org/10.1111/j.1365-2117.2006.00283.x

Coutand, I., Cobbold, P. R., Urreiztieta, M., Gautier, P., Chauvin, A., Gapais, D., et al. (2001). Style and history of Andean deformation, Puna Plateau, northwestern Argentina. *Tectonics*, *20*(2), 210–234. https://doi.org/10.1029/2000TC900031

Cristallini, E., Cominguez, A. H., & Ramos, V. A. (1997). Deep structure of the Metan-Guachipas region: Tectonic inversion in north-western Argentina. *Journal of South American Earth Sciences*, *10*(5–6), 403–421. https://doi.org/10.1016/S0895-9811(97)00026-6

Cristallini, E., Comnguez, A. H., Ramos, V. A., & Mercerat, E. D. (2004). *Basement double-wedge thrusting in the northern Sierras Pampeanas of Argentina (27°S)—Constraints from deep seismic reflection*. Tulsa, USA: The American Association of Petroleum Geologists (AAPG).

Dal Molin, C. N., Fernández, D., & Escosteguy, L. D. (2003). *Hoja Geologica 2766-IV*. Buenos Aires, Argentina: Concepción. Servicio Geológico Minero Argentino. Instituto de Geología y Recursos Minerales.

Dávila, F. M., Astini, R. A., Jordan, T. E., Gehrels, G., & Ezpeleta, M. (2007). Miocene forebulge development previous to broken foreland partitioning in the southern Central Andes, west-central Argentina. *Tectonics*, *26*, TC5016. https://doi.org/10.1029/2007TC002118

Davila, F. M., Gimenez, M. E., Nobile, J. C., & Martinez, M. P. (2012). The evolution of the high-elevated depocenters of the northern Sierras Pampeanas (ca. 28?? SL), Argentine broken foreland, South-Central Andes: The Pipanaco Basin. *Basin Research*, *24*(6), 615–636. https://doi.org/10.1111/j.1365-2117.2011.00539.x

DeCelles, P. G., Carrapa, B., Horton, B. K., & Gehrels, G. E. (2011). Cenozoic foreland basin system in the Central Andes of northwestern Argentina: Implications for Andean geodynamics and modes of deformation. *Tectonics*, *30*, TC6013. https://doi.org/10.1029/2011TC002948

DeCelles, P. G., Ducea, M. N., Kapp, P., & Zandt, G. (2009). Cyclicity in Cordilleran orogenic systems. *Nature Geoscience*, *2*(4), 251. Retrieved from–257. https://doi.org/10.1038/ngeo469

DeCelles, P. G., & Giles, K. A. (1996). Foreland basin systems. *Basin Research*, *8*(2), 105–123. https://doi.org/10.1046/j.1365-2117.1996.01491.x

del Papa, C., Hongn, F., Powell, J., Payrola, P., Do Campo, M., Strecker, M. R., et al. (2013). Middle Eocene–Oligocene broken-foreland evolution in the Andean Calchaqui Valley, NW Argentina: Insights from stratigraphic, structural and provenance studies. *Basin Research*, *25*(5), 574–593. https://doi.org/10.1111/bre.12018

Donelick, R. A., Ketcham, R. A., & Carlson, W. D. (1999). Variability of apatite fission-track annealing kinetics: II. Crystallographic orientation effects. *American Mineralogist*, *84*(9), 1213–1223. https://doi.org/10.2138/am-1999-0901

Dunkl, I. (2002). Trackkey: A windows program for calculation and graphical presentation of fission track data. *Computers and Geosciences*, *28*(1), 3–12. https://doi.org/10.1016/S0098-3004(01)00024-3

Encinas, A., Folguera, A. A., Oliveros, V. V., De Girolamo Del Mauro, L., Tapia, F., Riffo, R., et al. (2016). Late Oligocene–Early Miocene submarine volcanism and deep-marine sedimentation in an extensional basin of southern Chile: Implications for the tectonic development of the north Patagonian Andes. *Bulletin of the Geological Society of America*, *128*(5–6), 807–823. https://doi.org/10.1130/B31303.1

Faccenna, C., Oncken, O., Holt, A. F., & Becker, T. W. (2017). Initiation of the Andean orogeny by lower mantle subduction. *Earth and Planetary Science Letters*, *463*, 189–201. https://doi.org/10.1016/j.epsl.2017.01.041

Farley, K. A. (2002). (U-Th)/He dating: Techniques, calibrations, and applications. *Reviews in Mineralogy and Geochemistry*, *47*(1), 819–844. https://doi.org/10.2138/rmg.2002.47.18

Farley, K. A., Wolf, R. A., & Silver, L. T. (1996). The effects of long alpha-stopping distances on (U-Th)/He ages. *Geochimica et Cosmochimica Acta*, *60*(21), 4223–4229. https://doi.org/10.1016/S0016-7037(96)00193-7

Flowers, R. M. (2009). Exploiting radiation damage control on apatite (U–Th)/He dates in cratonic regions. *Earth and Planetary Science Letters*, *277*(1–2), 148–155. https://doi.org/10.1016/j.epsl.2008.10.005

Flowers, R. M., & Kelley, S. A. (2011). Interpreting data dispersion and "inverted" dates in apatite (U–Th)/He and fission-track datasets: An example from the US midcontinent. *Geochimica et Cosmochimica Acta*, *75*(18), 5169–5186. https://doi.org/10.1016/j.gca.2011.06.016

Flowers, R. M., Ketcham, R. A., Shuster, D. L., & Farley, K. A. (2009). Apatite (U–Th)/He thermochronometry using a radiation damage accumulation and annealing model. *Geochimica et Cosmochimica Acta*, *73*(8), 2347–2365. https://doi.org/10.1016/j.gca.2009.01.015

Flowers, R. M., Shuster, D. L., Wernicke, B. P., & Farley, K. A. (2007). Radiation damage control on apatite (U-Th)/He dates from the Grand Canyon region, Colorado Plateau. *Geology*, *35*(5), 447–450. https://doi.org/10.1130/G23471A.1

Galbraith, R. F., & Laslett, G. M. (1993). Statistical models for mixed fission track ages. *Nuclear Tracks and Radiation Measurements*, *21*(4), 459–470. https://doi.org/10.1016/1359-0189(93)90185-C

Gallagher, K. (2012). Transdimensional inverse thermal history modeling for quantitative thermochronology. *Journal of Geophysical Research*, *117*, B02408. https://doi.org/10.1029/2011JB008825

Gapais, D., Cobbold, P. R., Urreiztieta, M., Le Corre, C., & Rossello, E. (1996). Cenozoic dextral transpression and basin development at the southern edge of the Puna Plateau, northwestern Argentina. *Tectonophysics*, *254*(1–2), 17–39. https://doi.org/10.1016/0040-1951(95)00071-2

Georgieff, S. M., Ibañez, L. M., Vides, M. E., Anis, K. B., & Nieva, S. M. (2014). Paleógeno y Neógeno de Tucumán: Estratigrafía y paleoambientes sedimentarios. In *Geología de Tucumán* (pp. 106–123). San Miguel deTucumán, Argentina: Colegio de Graduados de Ciencias Geológicas de Tucumán.

Gianni, G. M., García, H. P. A., Pesce, A., Lupari, M., & Giambiagi, L. (2020). Oligocene to present shallow subduction beneath the southern Puna plateau. *Tectonophysics*, *780*, 228402. https://doi.org/10.1016/j.tecto.2020.228402

González, O. (2000). *Hoja Geológica 2766–11*. San Miguel de Tucumán: Servicio Geológico Minero Argentino, SEGEMAR.

Green, P. F. (1981). A new look at statistics in fission-track dating. *Nuclear Tracks*, *5*(1–2), 77–86. https://doi.org/10.1016/0191-278X(81)90029-9

Green, P. F., Duddy, I. R., Gleadow, A. J. W., Tingate, P. R., & Laslett, G. M. (1985). Fission-track annealing in apatite: Track length measurements and the form of the Arrhenius plot. *Nuclear Tracks and Radiation Measurements (1982)*, *10*(3), 323–328. https://doi.org/10.1016/0735-245X(85)90121-8

Grier, M. E., Salfity, J. A., & Allmendinger, R. W. (1991). Andean reactivation of the cretaceous Salta rift, northwestern Argentina. *Journal of South American Earth Sciences*, *4*(4), 351–372. https://doi.org/10.1016/0895-9811(91)90007-8

Haschke, M. R., Scheuber, E., Günther, A., & Reutter, K. J. (2002). Evolutionary cycles during the Andean orogeny: Repeated slab breakoff and flat subduction? *Terra Nova*, *14*(1), 49–55. https://doi.org/10.1046/j.1365-3121.2002.00387.x

Hongn, F., del Papa, C., Powell, J., Petrinovic, I., Mon, R., & Deraco, V. (2007). Middle Eocene deformation and sedimentation in the Puna-Eastern Cordillera transition (23°-26°S): Control by preexisting heterogeneities on the pattern of initial Andean shortening. *Geology*, *35*(3), 271–274. https://doi.org/10.1130/G23189A.1

Horton, B. K. (2018a). Sedimentary record of Andean mountain building. *Earth-Science Reviews*, *178*(November 2017), 279–309. https://doi.org/10.1016/j.earscirev.2017.11.025

Horton, B. K. (2018b). Tectonic regimes of the Central and Southern Andes: Responses to variations in plate coupling during subduction. *Tectonics*, *37*, 402–429. https://doi.org/10.1002/2017TC004624

Horton, B. K., & DeCelles, P. G. (1997). The modern foreland basin system adjacent to the Central Andes. *Geology*, *25*(10), 895–898. https://doi.org/10.1130/0091-7613(1997)025<0895:TMFBSA>2.3.CO;2

Hyland, E. G., Sheldon, N. D., & Cotton, J. M. (2015). Terrestrial evidence for a two-stage mid-Paleocene biotic event. *Palaeogeography, Palaeoclimatology, Palaeoecology*, *417*, 371–378. https://doi.org/10.1016/j.palaeo.2014.09.031

Iaffa, D. N., Sàbat, F., Muñoz, J. A., & Carrera, N. (2013). Basin fragmentation controlled by tectonic inversion and basement uplift in Sierras Pampeanas and Santa Bárbara System, Northwest Argentina. *Geological Society, London, Special Publications*, *377*(1), 101–117. https://doi.org/10.1144/sp377.13

Iaffa, D. N., Sàbat, F., Muñoz, J. A., Mon, R., Gutierrez, A. A., Iaffa, D. N., et al. (2011). The role of inherited structures in a foreland basin evolution. The Metán Basin in NW Argentina. *Journal of Structural Geology*, *33*(12), 1816–1828. https://doi.org/10.1016/j.jsg.2011.09.005

Jordan, T. E., & Allmendinger, R. W. (1986). The Sierras Pampeanas of Argentina: A modern analogue of Rocky Mountain foreland deformation. *American Journal of Science*, *286*(10), 737–764. https://doi.org/10.2475/ajs.286.10.737

Jordan, T. E., Isacks, B. L., Allmendinger, R. W., Brewer, J. A., Ramos, V. A., & Ando, C. J. (1983). Andean tectonics related to geometry of subducted Nazca plate. *Geological Society of America Bulletin*, *94*(3), 341–361. https://doi.org/10.1130/0016-7606(1983)94<341:ATRTGO>2.0.CO;2

Ketcham, R. A., Carter, A., Donelick, R. A., Barbarand, J., & Hurford, A. J. (2007). Improved modeling of fission-track annealing in apatite. *American Mineralogist*, *92*(5–6), 799–810. https://doi.org/10.2138/am.2007.2281

Ketcham, R. A., Donelick, R. A., & Carlson, W. D. (1999). Variability of apatite fission-track annealing kinetics: III. Extrapolation to geological time scales. *American Mineralogist*, *91*(2-3), 485–486. https://doi.org/10.2138/Am.2006.464

Kley, J., & Monaldi, C. R. (2002). Tectonic inversion in the Santa Barbara system of the central Andean foreland thrust belt, northwestern Argentina. *Tectonics*, *21*(6), 1061. https://doi.org/10.1029/2002TC902003

Kley, J., Monaldi, C. R., & Salfity, J. A. (1999). Along-strike segmentation of the Andean foreland: Causes and consequences. *Tectonophysics*, *301*(1–2), 75–94. https://doi.org/10.1016/S0040-1951(98)90223-2

Kley, J., Rossello, E. A., Monaldi, C. R., & Habighorst, B. B. (2005). Seismic and field evidence for selective inversion of Cretaceous normal faults, Salta rift, Northwest Argentina. *Tectonophysics*, *399*(1-4 SPEC. ISS), 155–172. https://doi.org/10.1016/j.tecto.2004.12.020

Kraemer, B., Adelmann, D., Alten, M., Schnurr, W., Erpenstein, K., Kiefer, E., et al. (1999). Incorporation of the Paleogene foreland into the Neogene Puna Plateau: The Salar de Antofalla area, NW Argentina. *Journal of South American Earth Sciences*, *12*(2), 157–182. https://doi.org/10.1016/S0895-9811(99)00012-7

Landtwing, M. R., Dillenbeck, E. D., Leake, M. H., & Heinrich, C. A. (2002). Evolution of the breccia-hosted porphyry Cu-Mo-Au deposit at Agua Rica, Argentina: Progressive unroofing of a magmatic hydrothermal system. *Economic Geology*, *97*(6), 1273–1292. https://doi.org/10.2113/97.6.1273

Löbens, S., Sobel, E. R., Bense, F. A., Wemmer, K., Dunkl, I., & Siegesmund, S. (2013). Refined exhumation history of the northern Sierras Pampeanas, Argentina. *Tectonics*, *32*, 453–472. https://doi.org/10.1002/tect.20038

Marquillas, R. A., del Papa, C., & Sabino, I. F. (2005). Sedimentary aspects and paleoenvironmental evolution of a rift basin: Salta Group (Cretaceous-Paleogene), northwestern Argentina. *International Journal of Earth Sciences*, *94*(1), 94–113. https://doi.org/10.1007/s00531-004-0443-2

Martinod, J., Gérault, M., Husson, L., & Regard, V. (2020). Widening of the Andes: An interplay between subduction dynamics and crustal wedge tectonics. *Earth-Science Reviews*, (march, *204*. https://doi.org/10.1016/j.earscirev.2020.103170

Morley, C. K., Haranya, C., Phoosongsee, W., Pongwapee, S., Kornsawan, A., & Wonganan, N. (2004). Activation of rift oblique and rift parallel pre-existing fabrics during extension and their effect on deformation style: Examples from the rifts of Thailand. *Journal of Structural Geology*, *26*(10), 1803–1829. https://doi.org/10.1016/j.jsg.2004.02.014

Mortimer, E., Carrapa, B., Coutand, I., Schoenbohm, L., Sobel, E. R., Gomez, J. S., & Strecker, M. R. (2007). Fragmentation of a foreland basin in response to out-of-sequence basement uplifts and structural reactivation: El Cajón–Campo del Arenal basin, NW Argentina. *Bulletin of the Geological Society of America*, *119*(5–6), 637–653. https://doi.org/10.1130/B25884.1

Moulin, M., Aslanian, D., & Unternehr, P. (2010). A new starting point for the south and equatorial Atlantic Ocean. *Earth-Science Reviews*, *98*(1–2), 1–37. https://doi.org/10.1016/j.earscirev.2009.08.001

Murray, K. E., Braun, J., & Reiners, P. W. (2018). Toward robust interpretation of low-temperature thermochronometers in magmatic terranes. *Geochemistry, Geophysics, Geosystems*, *19*, 3739–3763. https://doi.org/10.1029/2018GC007595

Oncken, O., Hindle, D., Kley, J., Elger, K., Victor, P., & Schemmann, K. (2006). Deformation of the Central Andean Upper Plate System—Facts, fiction, and constraints for plateau models. In *The Andes, Active Subduction Orogeny* (pp. 3–27). Berlin, Heidelberg: Springer. https://doi.org/10.1007/978-3-540-48684-8_1

Payrola, P., Powel, J. E., del Papa, C. E., & Hongn, F. (2009). Middle Eocene deformation-sedimentation in the Luracatao Valley: Tracking the initial Andean deformation in the Central Andes (NW Argentina). *Journal of South American Earth Sciences*, *28*, 142–154. https://doi.org/10.1016/j.jsames.2009.06.002

Pearson, D. M., Kapp, P., DeCelles, P. G., Reiners, P. W., Gehrels, G. E., Ducea, M. N., & Pullen, A. (2013). Influence of pre-Andean crustal structure on Cenozoic thrust belt kinematics and shortening magnitude: Northwestern Argentina. *Geosphere*, *9*(6), 1766–1782. https://doi.org/10.1130/GES00923.1

Pearson, D. M., Kapp, P., Reiners, P. W., Gehrels, G. E., Ducea, M. N., Pullen, A., et al. (2012). Major Miocene exhumation by fault-propagation folding within a metamorphosed, early Paleozoic thrust belt: Northwestern Argentina. *Tectonics*, *31*, TC4023. https://doi.org/10.1029/2011TC003043

Porto, J. C., Danieli, C. A., & Ruiz Huidobro, O. J. (1982). El Grupo Salta en la provincia de Tucumán, Argentina. In *V Congreso Latinoamericano de Geología. Actas* (Vol. 4, pp. 253–264). Buenos Aires, Argentina: Servicio Nacional Geológico Minero Argentino (SEGEMAR).

Ramos, V. A. (2008). The basement of the Central Andes: The Arequipa and related terranes. *Annual Review of Earth and Planetary Sciences*, *36*(1), 289–324. https://doi.org/10.1146/annurev.earth.36.031207.124304

Ramos, V. A. (2009). Anatomy and global context of the Andes: Main geologic features and the Andean orogenic cycle. *Geological Society of America Bulletin*, *204*, 31–66. https://doi.org/10.1130/2009.1204(02)

Ramos, V. A., Cristallini, E. O., & Pérez, D. J. (2002). The Pampean flat-slab of the Central Andes. *Journal of South American Earth*. Retrieved from http://www.sciencedirect.com/science/article/pii/S0895981102000068, *15*(1), 59–78. https://doi.org/10.1016/S0895-9811(02)00006-8

Ramos, V. A., & Folguera, A. (2009). Andean flat-slab subduction through time. *Geological Society, London, Special Publications*, *327*(1), 31–54. https://doi.org/10.1144/SP327.3

Reiners, P. W., & Brandon, M. T. (2006). Using thermochronology to understand orogenic erosion. *Annual Review of Earth and Planetary Sciences*, *34*(1), 419–466. https://doi.org/10.1146/annurev.earth.34.031405.125202

Reiners, P. W., & Farley, K. A. (2001). Influence of crystal size on apatite (U–Th)/He thermochronology: An example from the Bighorn Mountains, Wyoming. *Earth and Planetary Science Letters*, *188*(3–4), 413–420. https://doi.org/10.1016/S0012-821X(01)00341-7

Salfity, J. A., & Marquillas, R. A. (1994). Tectonic and sedimentary evolution of the Cretaceous-Eocene Salta Group basin, Argentina. In *Cretaceous tectonics of the Andes* (pp. 266–315). Wiesbaden, Germany: Springer.

Schmidt, C. J., Astini, R. A., Costa, C. H., Gardini, C. E., & Kraemer, P. E. (1995). Cretaceous rifting, alluvial fan sedimentation, and Neogene inversion, southern Sierras Pampeanas, Argentina. In *Petroleum Basins of South America* (pp. 341–358). Tulsa, US: AAPG. Memoir No. 62, (JANUARY).

Seggiaro, R., Caffe, P., Galli, C., Arnosio, M., & Da Poian, G. (2014). Evolución Tectónica Andina Entre Las Sierras De Hualfín, Capillitas Y Extremo Sur De Aconquija. *Revista de la Asociación Geológica Argentina*, *71*(4), 500–512. https://doi.org/10.1109/ICCE.2016.7430742

Shuster, D. L., Flowers, R. M., & Farley, K. A. (2006). The influence of natural radiation damage on helium diffusion kinetics in apatite. *Earth and Planetary Science Letters*, *249*(3–4), 148–161. https://doi.org/10.1016/j.epsl.2006.07.028

Sobel, E. R., Hilley, G. E., & Strecker, M. R. (2003). Formation of internally drained contractional basins by aridity-limited bedrock incision. *Journal of Geophysical Research*, *108*(B7), 2344. https://doi.org/10.1029/2002JB001883

Sobel, E. R., & Strecker, M. R. (2003). Uplift, exhumation and precipitation: Tectonic and climatic control of late Cenozoic landscape evolution in the northern Sierras Pampeanas, Argentina. *Basin Research*, *15*(4), 431–451. https://doi.org/10.1046/j.1365-2117.2003.00214.x

Sobolev, S. V., Babeyko, A. Y. Y., & Gruzinskaya, B. (2005). What drives orogeny in the Andes? *Geology*, *33*(8), 617–620. https://doi.org/10.1130/G21557.1

Strecker, M. R., Hilley, G. E., Bookhagen, B., & Sobel, E. R. (2011). Structural, geomorphic, and depositional characteristics of contiguous and broken foreland basins: Examples from the eastern flanks of the Central Andes in Bolivia and NW Argentina. In *Tectonics of sedimentary basins: Recent advances* (pp. 508–521). Chichester, UK: Blackwell Publishing.

Thiede, R. C., Bookhagen, B., Arrowsmith, J. R., Sobel, E. R., & Strecker, M. R. (2004). Climatic control on rapid exhumation along the Southern Himalayan Front. *Earth and Planetary Science Letters*, *222*(3–4), 791–806. https://doi.org/10.1016/j.epsl.2004.03.015

Vermeesch, P., Seward, D., Latkoczy, C., Wipf, M., Günther, D., & Baur, H. (2007). α-Emitting mineral inclusions in apatite, their effect on (U–Th)/He ages, and how to reduce it. *Geochimica et Cosmochimica Acta*, *71*(7), 1737–1746. https://doi.org/10.1016/j.gca.2006.09.020

Viramonte, J. G., Kay, S. M., Becchio, R., Escayola, M., & Novitski, I. (1999). Cretaceous rift related magmatism in central-western South America. *Journal of South American Earth Sciences*, *12*(2), 109–121. https://doi.org/10.1016/S0895-9811(99)00009-7

Wagner, G. A., Gleadow, A. J. W. W., & Fitzgerald, P. G. (1989). The significance of the partial annealing zone in apatite fission-track analysis: Projected track length measurements and uplift chronology of the transantarctic mountains. *Chemical Geology: Isotope Geoscience Section*, *79*(4), 295–305. https://doi.org/10.1016/0168-9622(89)90035-3

Yáñez, G., Cembrano, J., Pardo, M., Ranero, C., & Selles, D. (2002). The Challenger-Juan Fernández-Maipo major tectonic transition of the Nazca-Andean subduction system at 33–34°S: Geodynamic evidence and implications. *Journal of South American Earth Sciences*, *15*(1), 23–38. https://doi.org/10.1016/S0895-9811(02)00004-4

Zapata, S., Sobel, E. R., del Papa, C., Jelinek, A. R., & Glodny, J. (2019). Using a paleosurface to constrain low-temperature thermochronological data: Tectonic evolution of the Cuevas range, Central Andes. *Tectonics*, *38*, 3939–3958. https://doi.org/10.1029/2019TC005887

Zapata, S., Sobel, E. R., del Papa, C., Muruaga, C., & Zhou, R. (2019). Miocene fragmentation of the Central Andean foreland basins between 26 and 28°S. *Journal of South American Earth Sciences*, *94*, 102238. https://doi.org/10.1016/j.jsames.2019.102238

Zhou, R., Schoenbohm, L. M., Sobel, E. R., Davis, D. W., & Glodny, J. (2017). New constraints on orogenic models of the southern Central Andean Plateau: Cenozoic basin evolution and bedrock exhumation. *Bulletin of the Geological Society of America*, *129*(1-2), 152–170. https://doi.org/10.1130/B31384.1